






Systematic Bayesian Optimization for Atomic Structure Calculations of Heavy Elements

Ricardo Ferreira da Silva ^{1,2,*} Andreas Flörs ³ Luís Leitão^{1,2}
José P. Marques ^{1,2} Jorge M. Sampaio ^{1,2} and Gabriel Martínez-Pinedo ^{3,4}

¹*Laboratório de Instrumentação e Física Experimental de Partículas (LIP)*
Av. Prof. Gama Pinto 2, 1649-003 Lisboa, Portugal

²*Faculdade de Ciências da Universidade de Lisboa*
Rua Ernesto de Vasconcelos, Edifício C8, 1749-016, Lisboa, Portugal

³*GSI Helmholtzzentrum für Schwerionenforschung*
Planckstraße 1, D-64291, Darmstadt, Germany

⁴*Institut für Kernphysik (Theoriezentrum), Technische Universität Darmstadt*
Schlossgartenstraße 2, D-64289, Darmstadt, Germany

This study presents a novel optimisation technique for atomic structure calculations using the Flexible Atomic Code, focussing on complex multielectron systems relevant to r -process nucleosynthesis and kilonova modelling. We introduce a method to optimise the fictitious mean configuration used in the Flexible Atomic Code, significantly improving the accuracy of calculated energy levels and transition properties for lanthanide and actinide ions. Our approach employs a Sequential Model-Based Optimisation algorithm to refine the fictitious mean configuration, iteratively minimising the discrepancy between calculated and experimentally determined energy levels. We demonstrate the efficacy of this method through detailed analyses of Au II, Pt II, Pr II, Pr III, Er II, and Er III, representing a broad range of atomic configurations. The results show substantial improvements in the accuracy of the calculated energy levels, with average relative differences to the NIST data reduced from 20-60% to 10% or less for the ions studied. Transition wavelength calculations exhibit exceptional agreement with experimental data, with about 90% of the calculated values falling within 10% of measurements for Pr and Er ions. While improvements in transition probability calculations are observed, the calculated transition probabilities ($\log(gf)$ values) still show significant discrepancies compared to the experimental data, with root mean square deviations of approximately 1.1-1.4 dex for Pr and Er ions. We extend our optimisation technique to systematic calculations of singly and doubly ionised lanthanides, achieving accuracies comparable to or surpassing those of *ab-initio* atomic structure codes. The method's broad applicability across the lanthanide series demonstrates its potential for enhancing opacity calculations and spectral modelling in astrophysical contexts.

I. INTRODUCTION

Neutron star mergers have been confirmed to be sites of rapid neutron capture (r -process) nucleosynthesis, producing heavy elements beyond iron [1–5]. The electromagnetic counterpart to these events, known as kilonovae, provides a unique opportunity to study the creation and distribution of r -process elements [6]. Kilonova AT2017gfo has been extensively studied [7–11], indicating the presence of a wide range of r -process elements [12–23].

The modelling and interpretation of kilonova observations critically depend on accurate atomic data for r -process elements. Radiative transfer models require a comprehensive understanding of level energies and bound-bound atomic transitions, which account for most of the photon opacity in r -process-enriched ejecta [24]. Beyond one day after the merger, the ejecta mainly comprise neutral to four-times ionised atoms [25]. Lanthanide and actinide ions, characterised by their high-level density due to complex atomic structures with open

valence f -shells [26], are expected to contribute significantly to the opacity of the ejecta through numerous transitions. However, experimental data are available for only a small subset of these elements [27]. This scarcity of experimental data, coupled with the inherent complexity of these elements, poses significant challenges in atomic structure calculations. Consequently, theoretical atomic structure calculations are essential to provide a complete atomic data set of opacities for all ions of modelling interest, including particularly challenging actinides. Previous work has made significant progress in the calculation of atomic data for lanthanides and some actinides [28–35], demonstrating the critical role of accurate atomic data in understanding kilonova spectra and light curves. Nevertheless, highly accurate atomic structure calculations for these complex systems remain a challenging and time-consuming task, underscoring the need for continued refinement of computational methods.

However, recent observational advances have provided crucial insight into the composition of kilonovae. Multiple independent analysis of the spectra have identified strontium features (Sr, $Z = 39$) in the first days after the merger [15, 17]. Additional detections of elements on the left side of the periodic table, including zirconium (Zr, $Z = 40$) and lanthanides lanthanum (La, $Z = 57$)

* rfsilva@lip.pt

and cerium (Ce, $Z = 58$), have also been reported [19]. Preliminary efforts to identify gold and platinum have not succeeded, underscoring the persistent difficulties in identifying some of the most massive r -process elements within kilonova spectra [18, 36, 37].

Many approaches exist to perform atomic structure calculations, each offering different balances between accuracy and computational efficiency. The multiconfiguration Dirac-Fock method, implemented in codes such as GRASP2018 [38] and MCDFGME [39], can achieve high accuracy by optimising selected wavefunctions or minimising the energy function for individual or groups of levels. However, these calculations often come at the cost of significant computational time. Alternatively, codes like AUTOSTRUCTURE [40] and the Cowan suite of codes [41] employ very large configuration interaction (CI) expansions to achieve similar accuracy. These methods rely on radial wavefunctions derived from model potentials with scaling parameters, which are then fine-tuned based on available experimental data. Although this approach can help with accuracy, it requires careful adjustment and validation against known spectroscopic data. Recent work has shown promise in applying Bayesian machine learning techniques to optimise the scaling parameters of Slater-type orbitals used in the AUTOSTRUCTURE code. This technique was applied in the optimisation of orbital radial wavefunctions for neutral beryllium calculations [42, 43].

Finally, other codes such as HULLAC [44] and the Flexible Atomic Code (FAC) [45], rely on a local spherically averaged central potential to describe electron-electron and electron-nucleus interactions. Typically, this potential is derived from a fictitious mean configuration (FMC), assuming a uniform electron distribution. Although this approach simplifies calculations, it can introduce significant errors, particularly for near-neutral heavy elements with complex electron configurations, such as those found in the lanthanide and actinide series owing to the presence of open d and f shells.

The purpose of this study is to enhance the accuracy of atomic structure calculations by optimising the FMC. By refining the occupancy numbers of valence electrons, we seek to improve the agreement between the calculated energy levels and experimentally determined reference values. This optimisation employs a Sequential Model-Based Optimisation (SMBO) algorithm, implemented using the `scikit-optimize` (`skopt`) library in Python [46]. The SMBO algorithm is particularly effective for high-dimensional optimisation problems, balancing the exploration of new parameter spaces with the exploitation of known low-error regions.

Our methodology takes advantage of a carefully selected set of low-lying energy levels, either from experimental data or accurate *ab initio* calculations as benchmarks. These benchmarks guide the iterative refinement of the FMC, ultimately producing an optimised potential that significantly improves the fidelity of atomic structure calculations. The optimised FMC approach is not only

applicable to lanthanides and actinides but can be generalised to other elements and ionisation states, providing a robust tool for high-precision atomic data generation.

To demonstrate the effectiveness and versatility of our method, we present detailed analyses for selected ions across different elements and ionisation states. Specifically, we focus on Au II, Pt II, Pr II, Pr III, Er II, and Er III as case studies. These ions were chosen to represent a range of atomic structures and complexities. Au II and Pt II serve as benchmarks for our optimisations near the third r -process peak, which are of particular interest in kilonova spectra [18]. Pr II, Pr III, Er II, and Er III demonstrate the performance of the method across the lanthanide series, showcasing its applicability to different ionisation states and varying $4f$ shell complexities. By examining these diverse cases, we aim to illustrate the broad applicability of our optimised FMC approach and its potential to significantly enhance the accuracy of atomic structure calculations across the periodic table.

Our primary objective is to provide comprehensive atomic data for all lanthanide ions, addressing a critical need in the field of astrophysics and atomic physics. This data is essential for accurate modelling of kilonova spectra and for understanding the nucleosynthesis of heavy elements in neutron star mergers. By improving both the accuracy and efficiency of these calculations, we aim to enable more precise astrophysical modelling and potentially facilitate the identification of additional elements in future kilonova observations. Our optimisation procedure not only improves the accuracy of atomic structure calculations but also provides a crucial foundation for reliable level identification, which is essential for any subsequent energy level calibration against experimental data.

In the following sections, we will detail the computational procedures, describe the optimisation methodology, present the results of our calculations for the selected ions, and discuss their implications for astrophysical modelling and other applications requiring precise atomic data. We will also explore how this improved atomic data can contribute to our understanding of r -process nucleosynthesis and potentially aid in the identification of heavy elements in future kilonova observations.

II. ATOMIC STRUCTURE CALCULATIONS

The calculations in this work were performed using FAC (Flexible Atomic Code) [45]. FAC is an integrated software package for the calculation of various atomic structure and collisional processes based on a relativistic configuration interaction (RCI) method. In this method, the eigenstates are represented by atomic state functions Ψ which are constructed from a superposition of $i = 1, \dots, N_{\text{CSF}}$ configuration state functions (CSFs) φ_i

with the same total angular momentum J and parity P ,

$$\Psi(\gamma JM_J P) = \sum_i^{N_{\text{CSF}}} c_i \varphi_i(\gamma_i JM_J P), \quad (1)$$

where the γ_i encompasses all the remaining relevant information to define each CSF uniquely.

The mixing coefficients $\{c_i\}$ are obtained by solving the eigenvalue problem $\mathbf{H}\mathbf{c} = E\mathbf{c}$, with $\mathbf{c} = (c_1, c_2, \dots, c_{N_{\text{CSF}}})^t$. The eigenvalues obtained from the diagonalisation of the Hamiltonian matrix \mathbf{H} are therefore the best approximation for the energies in the space described by the selected CSFs. Although increasing the number of CSFs would improve the wave functions and the expected accuracy of the atomic energy levels (AELs), this improvement must be balanced against computational cost. Therefore, we determine an optimal set of CSFs by examining the energy level convergence with an increasing configuration basis.

FAC employs a variant of the conventional Dirac-Fock-Slater method to compute one-electron radial functions. Radial components are determined by solving the coupled Dirac equations self-consistently for a local central potential $V(r)$, following standard relativistic formulations [41]. A unique potential is used to derive the radial orbitals for the construction of basis states. As such, orthogonality is automatically ensured.

The local central potential includes contributions from both nuclear and electron-electron interactions. The nuclear contribution is modelled using a uniformly charged sphere with a radius determined by the atomic mass [45, 47]. For the electron-electron contribution, in the current version of FAC, contrary to earlier documentation, a Dirac-Fock-Slater (DFS) potential is implemented [48]

$$V_{ee}(r) = \sum_{\beta} \omega_{\beta} Y_{\beta,\beta}^0(r) - A\rho(r)^{1/3} \quad (2)$$

where $\beta = n'\kappa'$ defines the principal quantum number n' and relativistic quantum number κ' for each subshell and

$$Y_{\beta\eta}^{\lambda}(r) = \int_{r_{>}^{\lambda+1}}^{r_{<}^{\lambda}} \rho_{\beta\eta}(r') dr' \quad (3)$$

with $r_{<}^{\lambda} = \min(r, r')$, $r_{>}^{\lambda+1} = \max(r, r')$.

The first term represents the direct Coulomb interaction, spherically averaged over the bound electron states. Here $\omega_{\beta} = \omega_{n'\kappa'}$ are the occupation numbers for each subshell subject to $\sum \omega_{\beta} = N_e$, where N_e is the total number of electrons. An intrinsic feature of this Dirac-Slater approach is the inclusion of electron self-interaction, which manifests itself in the asymptotic behaviour $rV(r) \rightarrow N_e$ as $r \rightarrow \infty$, rather than the physically expected $N_e - 1$. While the self-interaction in the direct term is partially compensated for by including self-exchange in the second term of Equation (2), FAC additionally implements the Latter cut-off [49]

$$V(r) = \min\left(V(r), \frac{N_e - 1}{r}\right) \quad (4)$$

to ensure the correct asymptotic behaviour. The local exchange potential is given in terms of the total spherically averaged electron number density

$$\rho(r) = \frac{1}{4\pi r^2} \sum_{\beta} \omega_{\beta} \rho_{\beta}(r). \quad (5)$$

The coefficient A is simply a numerical factor pre-optimized for the ground configuration of each ion. This same approach has also been adopted in previous studies by Sampson *et al.* (2009) [50].

These occupation numbers ω_{β} are derived from a single fictitious mean configuration (FMC), ensuring a unique potential $V(r)$ for all electrons. Various methods can be used to determine the FMC occupation numbers. The FAC manual recommends distributing the occupation number of the electrons in the valence shells of the corresponding valence complex. Another approach involves splitting the occupancy number among a specific set of considered transitions, although this method is less computationally efficient [51, 52]. Both techniques have demonstrated effectiveness for highly ionised ions, where the wide level spacing and average screening effects yield reasonably accurate results.

Although these techniques are effective for highly ionised systems where the level spacing is wide and average screening effects dominate, they become less reliable for near-neutral ions, particularly lanthanides and actinides with open $4f$ and $5f$ shells. The exceptionally high density of energy levels in these systems, exceeding even the d block elements, makes the potential particularly sensitive to the screening contributions from electrons across different principal quantum numbers. This sensitivity motivates the optimisation procedure described in the following section.

III. FMC OPTIMISATION PROCEDURE

In this section, we present a method for optimising the local central potential in FAC, calculations by automatically adjusting the occupancy numbers of valence electrons. The method takes advantage of the relationship between the electron occupancy numbers ω_{β} and the local central potential $V(r)$, as described in Eq. (2). This relationship, while central to the accuracy of the calculations, cannot be directly determined. Instead, we treat it as a black-box function $\mathcal{F} : \{\omega_{\beta}\} \rightarrow V(r)$, which we seek to optimise by minimising the discrepancy between the calculated energy levels and the experimental reference data.

For near-neutral lanthanide and actinide ions, we focus on optimising the occupancy numbers of four key valence shells: the $4f$, $5d$, $6s$ and $6p$ orbitals for lanthanides, and $5f$, $6d$, $7s$ and $7p$ orbitals for actinides. These shells are chosen because they are close in energy and exhibit significant configuration mixing, leading to important contributions to the electron density in the valence region.

The f and d shells are particularly relevant because of their role in most of the low-lying configurations that dominate the atomic spectra.

The optimization is implemented using the Sequential Model-Based Optimisation (SMBO) algorithm through the `scikit-optimize` library in Python [46]. This approach is particularly effective for our four-dimensional optimization problem, as it efficiently balances the exploration of new parameter spaces with the exploitation of known low-error regions. To maintain physical relevance of our solutions, we constrain the occupancy numbers within specific bounds: the f -shell is restricted between $n_e - 2$ and $n_e + 2$, where n_e is the number of electrons in the ground configuration's f shell, allowing for physically reasonable excitations, while the outer p shells are limited between 0 and 1 reflecting their typical occupancy in excited configurations.

To evaluate different potentials produced by \mathcal{F} , we employ a sequential model-based optimisation (SMBO) approach. At each iteration, \mathcal{F} generates a potential $V(r)$ from a given set of $\{\omega_\beta\}$. This potential is used in the FAC calculations to produce energy levels, which are then compared to the experimental data. Although various statistical measures were considered for this comparison, the limited and nonuniform availability of experimental uncertainties for lanthanide and actinide energy levels made such approaches impractical. Instead, we found that a weighted root mean square deviation (WRMSD) provided the most reliable convergence:

$$\mathcal{L}_{\text{weighted}} = \sqrt{\frac{1}{N} \sum_{i=1}^N e^{-E_i^{\text{ref}}/kT} (\Delta E_i)^2}, \quad (6)$$

where ΔE_i is the difference between the calculated and reference energy levels. The Boltzmann factor $e^{-E_i^{\text{ref}}/kT}$ accounts for the thermal population distribution under local thermodynamic equilibrium conditions, which makes optimisation particularly relevant for kilonova modelling. While other metrics such as weighted average deviation and level density were tested, WRMSD provided better convergence with fewer iterations. Using A-values or oscillator strengths as evaluation metrics was considered but rejected as it would require computing these values at each iteration, significantly increasing the computational time.

It is important to note that perfect agreement for all energy levels simultaneously cannot be guaranteed, as this is fundamentally limited by the local central potential approximation used in FAC. Different energy levels might require different optimisation parameters for the best agreement, creating an inherent trade-off in the optimisation process. This limitation of the model is particularly evident in cases with strong configuration mixing, where the mean-field approach might not capture all correlation effects adequately. Our optimisation strategy therefore aims to find the best compromise solution that improves overall agreement while maintaining physical relevance.

The optimisation process requires balancing exploration of unknown regions with exploitation of known good solutions. This balance is achieved through three complementary acquisition functions: Lower Confidence Bounds (LCB), Expected Improvement (EI), and Probability of Improvement (PI). These functions are computed concurrently, with LCB focussing on the trade-off between predicted mean and uncertainty, EI targeting potential improvements over the current best solution, and PI evaluating the probability of finding better solutions. A GP-Hedge portfolio strategy [53] probabilistically selects among them using a softmax function, ensuring robust exploration of the parameter space while efficiently converging to optimal solutions.

Optimisation begins with the initial values $\{\omega_\beta\}$ derived from the first few energetically ordered configurations, ensuring convergence to physically meaningful values. Subsequent points are chosen using Latin hypercube sampling, which ensures efficient coverage of the parameter space by stratifying the sampling regions. A Gaussian surrogate model approximates \mathcal{F} , creating an effective four-dimensional surface that guides optimisation. The model is updated after each evaluation to incorporate new information and guide the selection of subsequent points in the parameter space. The process typically converges within 50-100 iterations, with individual evaluations ranging from seconds to half an hour depending on the basis set size. The optimisation procedure follows these key steps:

1. **Data Collection:** Gather reference data from experimental measurements or accurate *ab initio* calculations. This data must include the first few low-lying energy levels.
2. **Initial Calculations:** Perform initial calculations of energy levels using a restricted basis set. These calculations provide a preliminary set of results based on the initial FMC.
3. **Evaluation of Results:** Compare the calculated energy levels with the reference data. The evaluation is performed using a loss function, such as WRMSD, which quantifies the difference between the calculated and reference levels.
4. **Update Surrogate Model:** Based on the evaluation, update the surrogate model that approximates the objective function. This model guides the optimisation process by predicting the impact of changes in the FMC on the calculated energy levels.
5. **Recalculate FMC:** Use the updated surrogate model to calculate a new FMC that minimises the difference between the calculated and reference energy levels.
6. **Convergence Check:** Convergence is verified by evaluating whether changes in the FMC lead to a

significant improvement in the calculated energy levels. If convergence is not achieved, repeat the process from the evaluation step.

7. **Final Calculation:** Once convergence is achieved, perform a full calculation using the optimised FMC and an extended basis set. This final step ensures the convergence of the calculation for a higher number of CSFs, without compromising the computational time in the previous steps.

This methodology is general and can be adapted to other atomic structure codes, with the flexibility to modify the loss function for different optimisation needs. The systematic evaluation of the predicted atomic data' sensitivity to the optimised mean local potential provides valuable insights into the reliability and precision of the results.

IV. BENCHMARK OF OPTIMISATION PROCEDURE

In this section, we present the benchmarking of our atomic structure calculations using FAC, focussing on the energy levels and electric dipole (E1) transitions for selected elements. The elements chosen for this study are Au II, Pt II, and lanthanides Pr II, Pr III, Er II, Er III. For each element, we compare our calculated data with reference data from the NIST Atomic Spectra Database (ASD)[27] and other recent experimental and theoretical studies. The results are presented, when appropriate with energy level labels using both LS and jj coupling schemes. In the jj coupling notation, the label is denoted as $(j_1, j_2, \dots)_J$, where j are the total angular momenta of individual shells and J is the total angular momentum of the configuration. While FAC naturally produces results in jj coupling, we employ the JJ2LSJ program [54] to obtain the LS coupling labels. The identification of calculated levels with NIST experimental data was performed by matching total angular momentum J and parity quantum numbers, and using the energy ordering within each J -parity group, similarly to what has been done in previous work [35].

A. Au II and Pt II

The motivation for studying Au II and Pt II arises from their potential relevance in kilonova spectra, particularly the kilonova associated with GW170817. The presence of these elements can provide critical insights into the conditions and processes occurring in outflows from neutron star mergers. Additionally, benchmarking the optimisation procedure against non-rare earth elements like Au and Pt validates our methods in a broader context.

1. Available data

The data available in the NIST ASD served as the reference dataset for both Au II and Pt II. For Au II, the dataset includes energy levels and transition probabilities compiled from Moore (1971)[56], Rosberg and Wyart (1997) [57], and Sansonetti and Martin (2005) [58]. Moore provides a compilation of atomic energy levels derived from optical spectra, including detailed information on the energy levels of Au II obtained through spectroscopic observations and measurements. Rosberg and Wyart conducted a study on the spectrum of Au II using Fourier transform spectroscopy and photographic spectrograms. Their research identified 75 new energy levels for Au II. This data was then consolidated in Sansonetti and Martin's handbook of basic atomic spectroscopic data, which is available through the NIST database.

For Pt II, extensive data is available from several key studies. Reader et al. (1988) [59] provided accurate energy levels for singly ionised platinum (Pt II) by observing the spectrum with hollow-cathode lamps and using a Fourier-transform spectrometer. Their work resulted in the measurement of 558 lines and the determination of accurate values for 28 even and 72 odd energy levels. Blaise and Wyart (1992)[60] further contributed to the understanding of Pt II energy levels by compiling extensive experimental data, which included the use of both classical emission spectroscopy and Fourier-transform spectroscopy. They presented revised energy levels, new classifications, and improved wavelengths for numerous transitions, significantly enhancing the accuracy and consistency of the dataset. Furthermore, Wyart, Blaise, and Joshi (1995)[61] conducted a theoretical study of the odd parity levels and transition probabilities in Pt II. They employed Hartree-Fock relativistic calculations with configuration interaction to predict energy levels and transition probabilities, providing essential theoretical insights to complement the experimental findings and addressing discrepancies in earlier experimental data.

2. Computational procedure

The first stage involved determining the optimal FMC using a reference dataset of accurately determined low-lying levels from the NIST ASD. The basis space for Au II and Pt II was then expanded to include all major configurations up to the ionisation energy.

For both ions, the configurations employed in the calculations were generated using single (S) and double (D) excitations from the ground state of each respective ion, extending up to $\{8s, 8p, 7d, 6f, 5g\}$. FAC was used to perform the calculations both with and without FMC optimisation to assess the impact of the optimisation process on the accuracy of the results. Comparison with experimental data was performed by calculating the relative

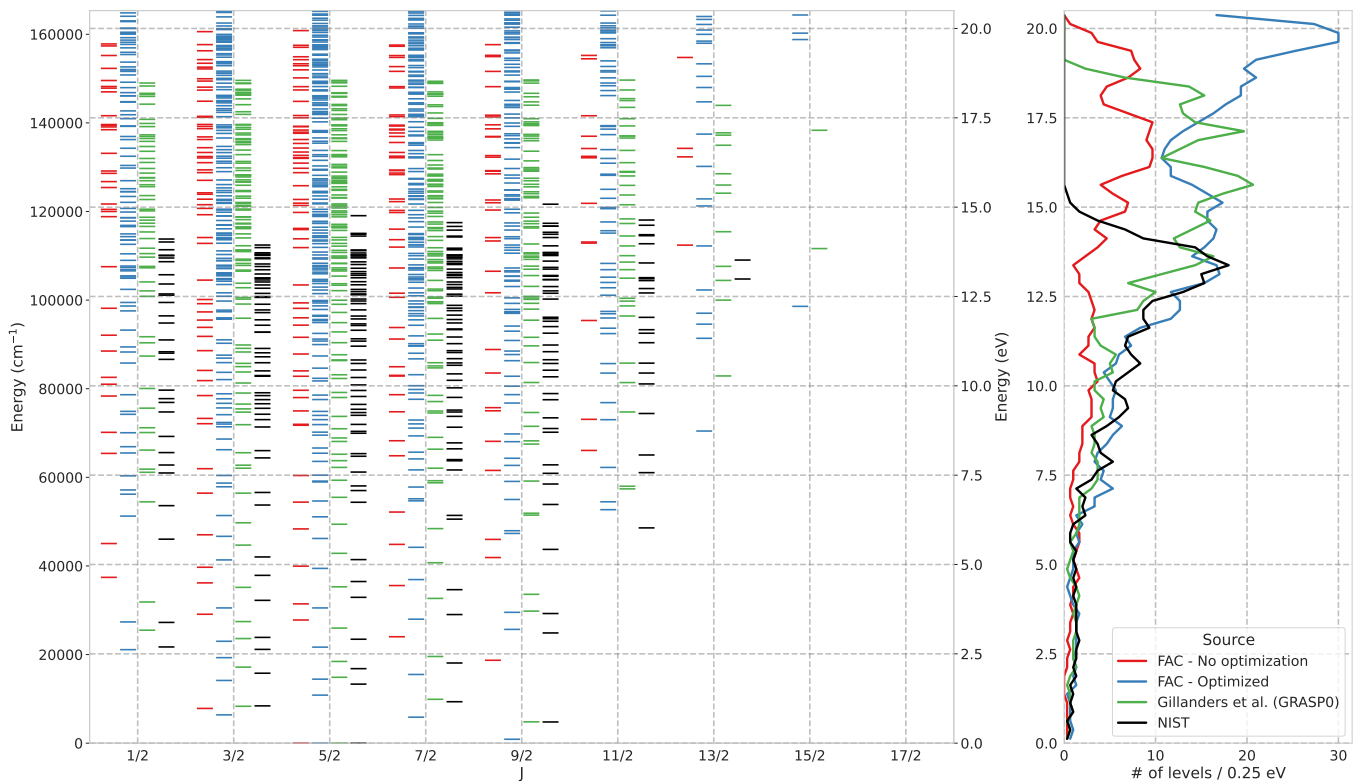


FIG. 1. Energy levels of Pt II. Black horizontal lines show the data from the NIST ASD [27]. Coloured horizontal lines show the calculated data using FAC with (blue) and without (red) the optimisation procedure, and using GRASPO (green), which was used in [18].

difference in excitation energies:

$$\Delta E_{\text{rel}} = \frac{E_{\text{FAC}} - E_{\text{NIST}}}{E_{\text{NIST}}} \quad (7)$$

where E_{FAC} and E_{NIST} are the excitation energies from our calculations and the NIST database, respectively.

Core-core and core-valence correlations were not included due to computational constraints. The impact of the optimisation was evaluated through direct comparison with the available experimental data.

3. Energy Levels

Figures 1 and 2 provide a comprehensive comparison of the energy levels for each angular momentum, J , for Pt II and Au II, respectively. The benchmark data from NIST ASD are compared with the results of our calculations using FAC as well as the energy levels reported by Gillanders et al. using the GRASPO code [18]. In particular, the comparison is done for each $2J$ value and is not divided by parity, as the data obtained from Gillanders et al. did not include information on configurations or parity. This comparison highlights the effectiveness of the FMC optimisation in aligning our calculated energy levels with the NIST reference data, demonstrating significant improvements over the non-optimised results. For

the non-optimised model, the electron occupancy number FMC was taken from an average using the ground and first configuration in energy, this is $5d^9$ and $5d^8 6s$ for Pt II and $5d^{10}$ and $5d^9 6s$ for Au II, applying the standard semi-empirical correction built into the code. In particular, for the lowest levels, the optimised results show a typical differences in excitation energy of less than 10% compared to the experimental data from NIST, in line with the results obtained for GRASPO for the singly-ionised species. These results highlight the impact of the optimisation, particularly for low-lying levels with excitation energies below 7.5 eV, where large differences are found compared to the *default* FAC calculation. The comparison illustrates the substantial improvement in accuracy of the excitation energies achieved through the optimisation process.

Figure 3 illustrates the average relative difference to the data available in the NIST ASD for all identified levels of Pt II and Au II for different models computed with the FAC. The “No Opt.” model corresponds to an 8-configuration model that does not use the FAC potential optimisation, whereas the other models incorporate the optimisation. The impact of the optimisation is significant, resulting in a much greater improvement which was not achievable just by the inclusion of a larger CI basis. The results of the optimised models show a closer alignment to the NIST reference data, demonstrating similar

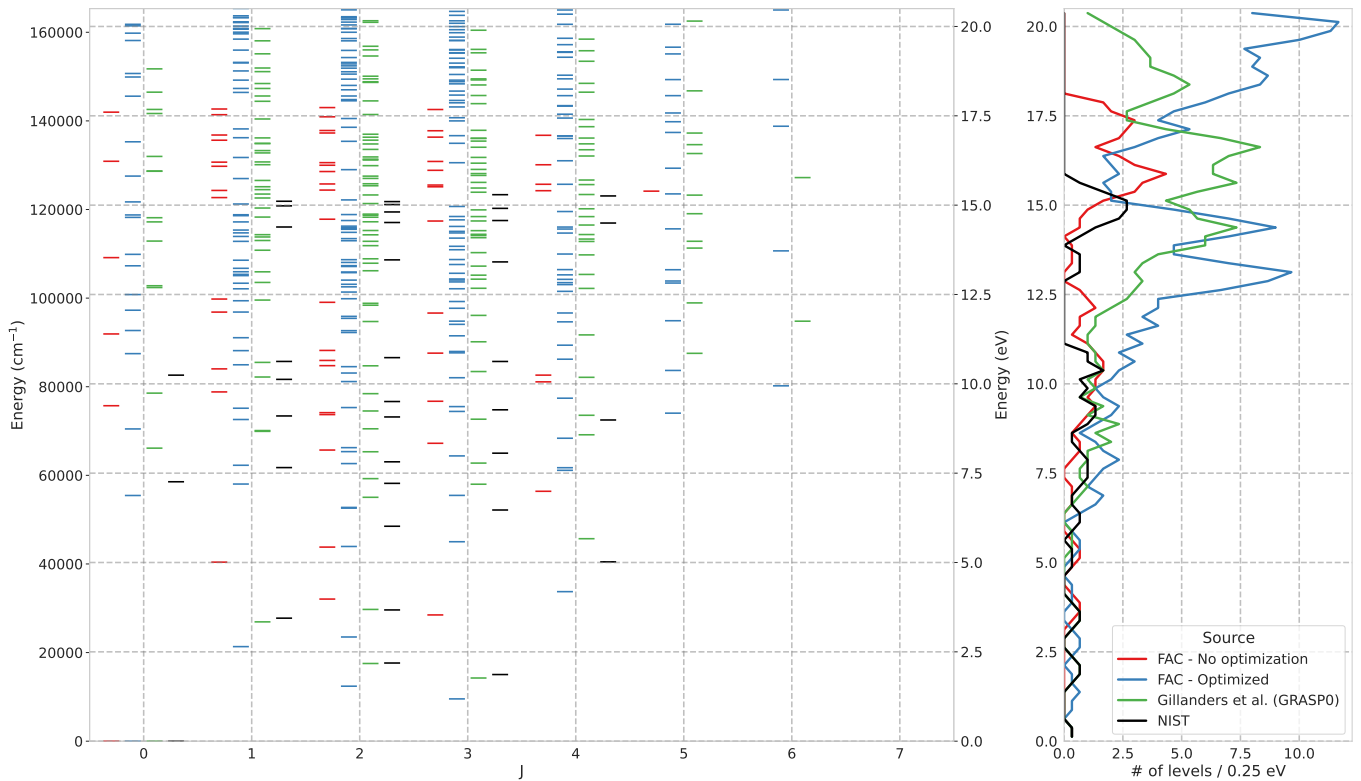


FIG. 2. Energy levels and level density of Au II. Black horizontal lines show the data from the NIST ASD [27]. Coloured horizontal lines show the calculated data using FAC with (blue) and without (red) the optimisation procedure, and using GRASPO (green), which was used in [18].

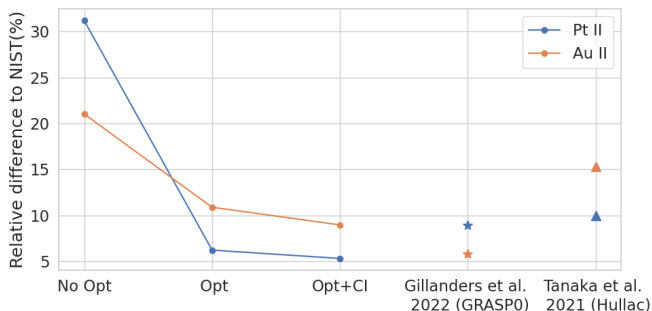


FIG. 3. Average relative difference to the data available in the NIST ASD [27] for all identified levels of Pt II and Au II for the different models computed with FAC. “No Opt.” corresponds to an 8 configuration model that does not use the FAC potential optimisation, contrarily to the other two models. The results are compared with the results from GRASPO [18] and HULLAC [28, 55], available in the literature.

accuracy to the GRASPO [18] results and better energy than the HULLAC results [28, 55].

B. Pr II and Pr III

1. Available data

A first study on the spectrum of singly-ionised praseodymium was conducted by Rosen et al. (1941) [62], which determined energies, g and J values for 74 levels from resolved Zeeman patterns of 141 lines in the UV and optical range (2400 to 7100 Å). Ginibre (1989) [63] studied 105 odd and 187 even experimental energy levels using Fourier transform (FT) spectroscopy over the range of 2783–25 000 cm^{-1} . Furthermore, Wyart et al. (1974) [64] studied a significant number of levels corresponding to the $4f^N(5d+6s)$ configurations for multiple lanthanides, including Pr II and Pr III. Later, LS-coupling labelling was assigned to many of the identified levels using a semi-empirical fitting approach by Ginibre (1990) [65]. Later experimental measurements were conducted by Ivarsson et al. (2001) [66], which adjusted the energy of 39 levels using FT spectroscopy in the 2800–8000 Å range. Furmann et al. (2005, 2007) [67, 68] examined 31 odd and 14 even levels using laser-induced fluorescence (LIF) spectroscopy in a hollow cathode discharge lamp. More recently, Akhtar & Windholz (2012) [69] re-evaluated the energy values for 227 levels (74 odd and 153 even parity) and the hyperfine structures of 477 transi-

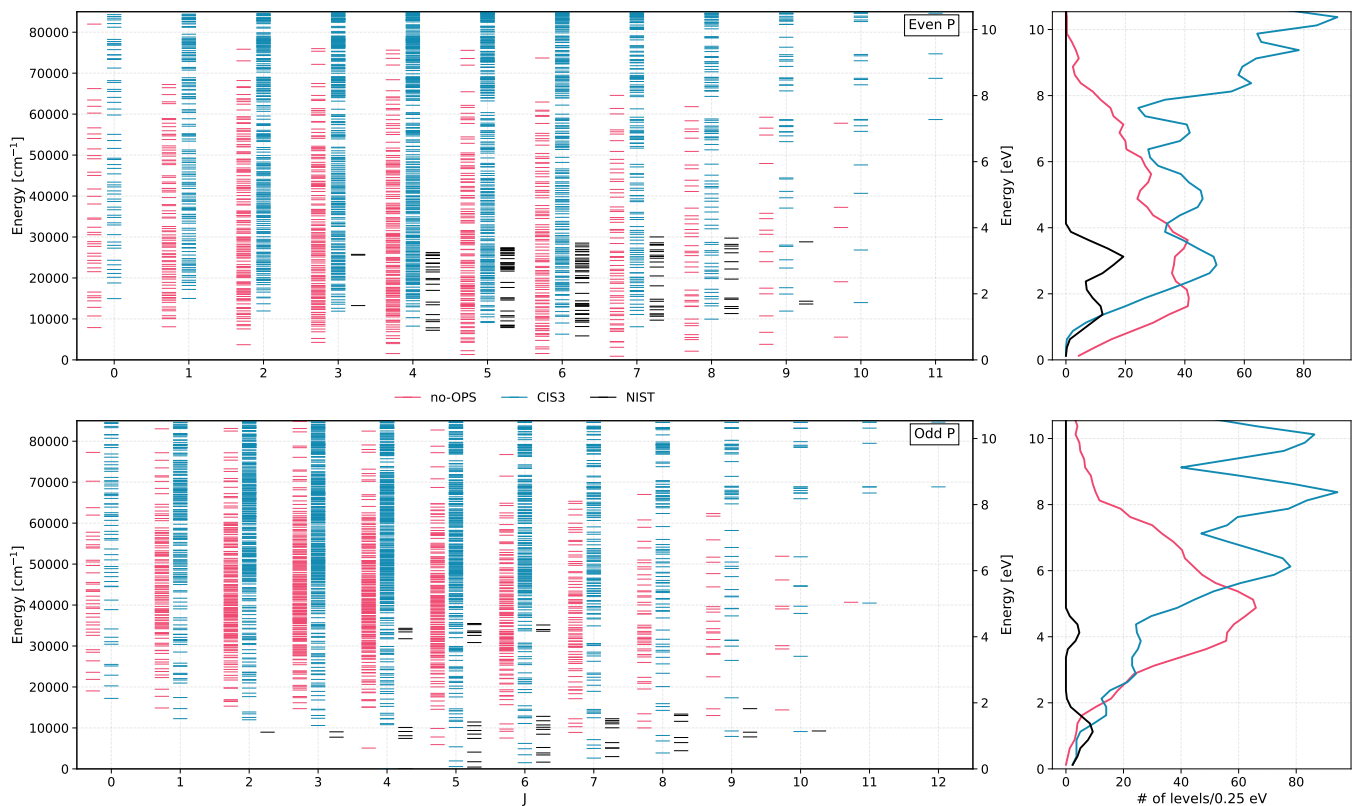


FIG. 4. Energy levels of and level density Pr II. Results for a calculation without optimization of the FMC (using a set of configurations equivalent to OPS) are shown alongside the results for our largest calculation, including the optimization. Black horizontal lines show the data from the NIST ASD [27].

tions in the 3260–11700 Å range, correcting the energy levels from Ginibre and Ivarsson et al. All these levels were measured or reanalysed with high precision. The data from these studies are summarised in [70, Martin et al. (1978)], and this work is included in the NIST ASD.

2. Computational procedure

The first stage involved computing the FMC used to determine the optimal potential. This was done using a reference dataset that included at least a few accurately determined low-lying levels. The data from the NIST ASD was used as the main reference for building this dataset.

The basis space for Pr II and Pr III was expanded to include all major configurations up to the ionisation energy. For Pr II and Pr III, it was found that considering SD excitations from the ground configuration ($4f^3 6s$ for Pr II and $4f^3$ for Pr III) up to $7s, 7p, 7d, 5f, 5g$ effectively covered the most relevant configurations that contribute directly to opacity [35]. These configurations were used in the optimisation procedure in order to determine the optimal FMC for these ions. Hence, we label this space as Optimisation Space (OPS). To further enhance the convergence of the results, additional configurations were in-

cluded based on SD excitations extending up to principal quantum number $n = 10$ angular momentum $\ell = 5$. The space was increased in multiple steps from a base ground configuration (GC), with each space used labelled as a different CI space (CIS). The scheme for the full set of calculations was as follows.

- OPS = GC + SD{ $7s, 7p, 7d, 5f, 5g$ }
- CIS1 = OPS + SD{ $8s, 8p, 8d, 6f, 5g$ }
- CIS2 = CIS1 + SD{ $9s, 9p, 9d, 7f, 6g$ }
- CIS3 = CIS2 + SD{ $10s, 10p, 10d, 7f, 6g$ }

While core-core and core-valence correlations are expected to improve the calculations for these ions [71], they were found to be too computationally demanding. Moreover, the marginal improvements in accuracy potentially gained from these correlations may not justify the significant increase in computational resources required.

3. Energy Levels

The energy levels computed for Pr II and Pr III are compared with the NIST recommended values in Figures Fig. 4 and Fig. 5. The results without optimisation

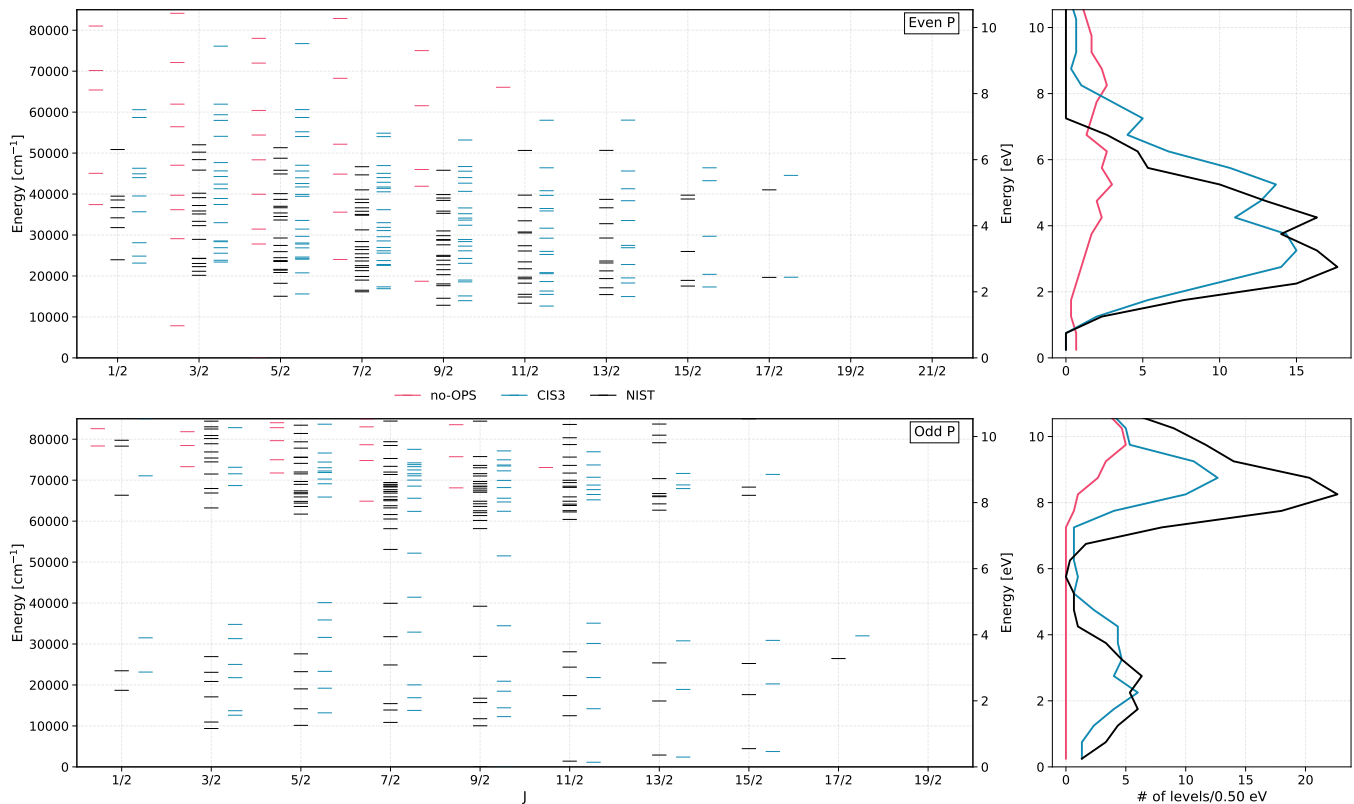


FIG. 5. Energy levels of and level density Pr III. Results for a calculation without optimization of the FMC (using a set of configurations equivalent to OPS) are shown in pink alongside the results for our most complete calculation for Pr III, in blue, including the optimization. Black horizontal lines show the data from the NIST ASD [27].

(using a set of configurations equivalent to OPS) show a significant deviation from the NIST values, with an average relative difference of approximately 60% for Pr II and 20% for Pr III. The optimised results, however, show a marked improvement, reducing the average relative difference to about 10% for Pr II and 8% for Pr III. The black horizontal lines show the data from the NIST ASD. This improvement underscores the efficacy of the FMC optimisation in enhancing the accuracy of our computed energy levels. Additionally, the results indicate that the optimised configurations effectively capture the electron correlation effects, which are crucial for achieving close agreement with the experimental data.

By examining the figures, it is evident that the optimisation particularly benefits the lower energy levels, whereas the non optimised results tend to diverge more significantly from the NIST values. This trend is consistent across both Pr II and Pr III, highlighting the robustness of the optimisation approach. The figures also demonstrate that the higher energy levels, while improved, still exhibit some discrepancies. These discrepancies can be attributed to the higher energy levels being more scarce and often isolated in the NIST database (e.g., odd parity Pr II), which may or may not allow great results for these levels.

The average relative difference from the NIST data for

all identified levels of Pr II and Pr III for the different models calculated with FAC is shown in Fig. 6. The “No Opt.” model corresponds to the OPS configuration model that does not use the FAC potential optimisation, whereas the other models incorporate this optimisation. The optimisation leads to a substantial reduction in the relative difference, far exceeding the improvements achieved by CI alone. Additionally, the convergence of results across different CI spaces (CIS1, CIS2, and CIS3) indicates that the optimisation process stabilises the calculations, ensuring reliable and consistent results. The results for the energy levels of the first 20 computed levels are shown in Tables I and II.

4. Transitions

To evaluate the accuracy of our calculations for transition probabilities and wavelengths in Pr II and Pr III, we compared our results with recent experimental data from Ferrara et al. (2024) [72]. Their study provides valuable spectroscopic data for several high- Z elements, including praseodymium, covering the 3700-10000 Å range using high-resolution échelle spectroscopy. Figure 7 presents a comparison between the calculated $\log(gf)$ values from our CIS3 model and the experimental data. The exper-

TABLE I. Energy levels (in cm^{-1}) for the first 20 levels of Pr II. The columns show: electronic configuration (Config.), level labels in LS and jj coupling, calculated energies without optimization ($E_{\text{no-OPS}}$), with optimization space only (E_{OPS}), and with increasing configuration interaction spaces (E_{CIS1} , E_{CIS2} , E_{CIS3}). The experimental values from NIST (E_{NIST}) and relative differences between CIS3 and experimental values (Δ_{CIS3}) are given in the last two columns.

Config.	LSJ	jj	$E_{\text{no-OPS}}$	E_{OPS}	E_{CIS1}	E_{CIS2}	E_{CIS3}	E_{NIST}	$\Delta_{\text{CIS3}}(\%)$
$4f_3 6s$	5I_4	$(9/2, 1/2)_4$	5080.19	0.00	0.00	0.00	0.00	0.00	—
$4f_3 6s$	5I_5	$(9/2, 1/2)_5$	5925.82	591.86	589.12	592.23	566.52	441.95	28.19%
$4f_3 6s$	5I_6	$(11/2, 1/2)_6$	7532.35	1746.43	1810.25	1707.48	1512.49	1649.01	8.28%
$4f_3 6s$	3I_5	$(11/2, 1/2)_5$	7786.34	2012.86	1998.63	2007.36	1942.94	1743.72	11.42%
$4f_3 6s$	5I_7	$(13/2, 1/2)_7$	8902.52	3554.95	3114.87	3073.74	2634.58	2998.36	12.13%
$4f_3 6s$	3I_6	$(13/2, 1/2)_6$	9726.35	3699.41	3778.21	3532.30	3445.13	3403.21	1.23%
$4f_3 5d$	5L_6	$(9/2, 3/2)_6$	9179.41	5158.62	5115.33	5052.51	4915.09	3893.46	26.24%
$4f_3 5d$	5K_5	$(9/2, 3/2)_5$	17789.41	5595.43	5590.27	5649.02	5393.42	4097.60	31.62%
$4f_3 6s$	5I_8	$(15/2, 1/2)_8$	10004.31	4669.32	4744.13	4675.17	3883.28	4437.15	12.48%
$4f_3 6s$	3I_7	$(15/2, 1/2)_7$	11159.94	5776.56	5652.82	5217.45	4995.07	5079.35	1.66%
$4f_3 5d$	5L_7	$(11/2, 3/2)_7$	18355.79	6083.82	5912.63	6010.73	5814.83	5108.40	13.83%
$4f_3 5d$	5K_6	$(11/2, 3/2)_6$	16917.59	6489.45	6517.05	6306.81	6217.95	5226.52	18.97%
$4f_2 5d_2$	5L_6	$(4, 6)_6$	5755.23	6569.53	6553.05	6402.30	6280.25	5854.61	7.27%
$4f_3 5d$	5L_7	$(11/2, 5/2)_7$	10297.00	7306.01	7416.36	7498.47	7142.73	6413.93	11.36%
$4f_3 5d$	5K_8	$(11/2, 5/2)_8$	21291.86	6960.23	7027.83	6999.42	6820.46	6417.83	6.27%
$4f_2 5d_2$	3I_4	$(5, 7)_4$	7483.54	8491.31	8251.76	8568.32	8238.45	7227.99	13.98%
$4f_3 5d$	5G_5	$(9/2, 5/2)_5$	16576.42	10452.05	10587.04	10426.38	10114.77	7438.23	35.98%
$4f_3 5d$	5I_4	$(9/2, 5/2)_4$	15049.01	11302.87	10910.87	11116.26	10788.88	7446.43	44.89%
$4f_3 5d$	5K_8	$(13/2, 5/2)_8$	13454.15	8410.92	8765.74	8267.51	8158.91	7659.76	6.52%
$4f_3 5d$	3H_3	$(9/2, 5/2)_3$	14705.94	10817.93	10830.89	11031.73	10595.78	7744.27	36.82%

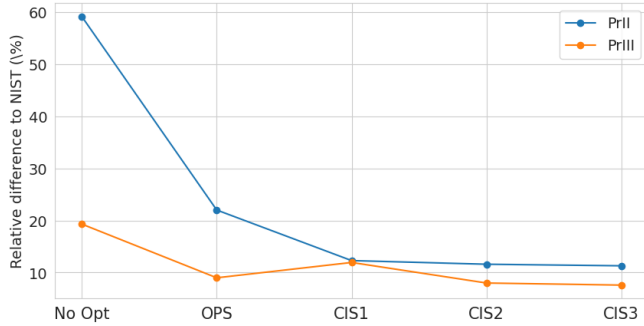


FIG. 6. Average relative difference to the data available in the NIST ASD [27] for all identified levels of Pr II and Pr III for all the different models computed with FAC. “No Opt.” corresponds to an OPS configuration model that does not use the FAC potential optimisation, contrary to the other models.

imental values are derived using two methods: Boltzmann plots and cascade calculations. It’s important to note that while cascade method results are generally reliable within the limits of adopted literature values, the Boltzmann method is only valid for transitions in thermodynamic equilibrium. When available, we also evaluated our data against data from the Vienna Atomic Line Database (VALD) [73]. As evident from Fig. 7, there is considerable scatter in the $\log(gf)$ values, particularly

for weaker transitions ($\log(gf) < -2$). The agreement between our calculations and the experimental data improves for stronger transitions, but discrepancies persist across the entire range. Quantitatively, we observe a root mean square deviation (RMSD) of approximately 1.1 dex between our calculated $\log(gf)$ values and the experimental data. This level of disagreement is not uncommon in atomic structure calculations for complex ions like Pr II and Pr III, especially given the challenges in accurately representing the electron correlations in these systems. In contrast, Fig. 8 shows excellent agreement between our calculated wavelengths and the experimental values. Most of the calculated wavelengths fall within 10% of the experimental data, as indicated by the points between the inner dotted lines. Nearly all calculated wavelengths are within 20% of the experimental values, falling between the dashed lines. Quantitatively, we find that approximately 80% of our calculated wavelengths deviate less than 20% from the experimental values and 96% are within 10%. This disparity in accuracy between the transition probabilities and wavelengths is a common feature in atomic structure calculations. Wavelengths, which are primarily determined by energy level differences, are often more accurately predicted than transition probabilities, which depend on the precise details of the wavefunctions.

TABLE II. Energy levels (in cm^{-1}) for the first 20 levels of Pr III. The columns show: electronic configuration (Config.), level labels in LS and jj coupling, calculated energies without optimization ($E_{\text{no-OPS}}$), with optimization space only (E_{OPS}), and with increasing configuration interaction spaces (E_{CIS1} , E_{CIS2} , E_{CIS3}). The experimental values from NIST (E_{NIST}) and relative differences between CIS3 and experimental values ($\Delta_{\text{CIS3}}(\%)$) are given in the last two columns.

Config.	LSJ	jj	$E_{\text{no-OPS}}$	E_{OPS}	E_{CIS1}	E_{CIS2}	E_{CIS3}	E_{NIST}	$\Delta_{\text{CIS3}}(\%)$
$4f_3$	$^4I_{9/2}$	$(9/2)_{9/2}$	0.00	0.00	0.00	0.00	0.00	0.00	—
$4f_3$	$^4I_{11/2}$	$(11/2)_{11/2}$	1326.93	1592.85	1352.95	1357.94	1331.27	1398.34	4.80%
$4f_3$	$^4I_{13/2}$	$(13/2)_{13/2}$	2427.11	3054.46	2812.87	2767.48	2601.63	2893.14	10.08%
$4f_3$	$^4I_{15/2}$	$(15/2)_{15/2}$	3247.11	4713.66	5393.79	4112.37	4983.26	4453.76	11.89%
$4f_3$	$^4F_{3/2}$	$(3/2)_{3/2}$	11040.02	8700.01	9100.72	9704.16	10040.01	9370.66	7.14%
$4f_3$	$^4S_{5/2}$	$(5/2)_{5/2}$	11715.30	9501.93	7914.18	10433.33	10355.69	10138.18	2.15%
$4f_3$	$^2H_{7/2}$	$(7/2)_{7/2}$	12256.66	11283.33	12769.56	12425.54	9712.14	10859.06	10.56%
$4f_3$	$^4F_{3/2}$	$(3/2)_{3/2}$	12113.48	9868.64	11256.59	12871.12	9985.74	10950.24	8.81%
$4f_3$	$^2H_{9/2}$	$(9/2)_{9/2}$	12775.43	12744.02	12852.55	12138.72	11314.66	11761.69	3.80%
$4f_3$	$^2G_{11/2}$	$(11/2)_{11/2}$	12417.17	10997.75	14184.62	11278.18	13289.73	12494.63	6.36%
$4f_2 5d$	$^4D_{9/2}$	$(4, 3/2)_{9/2}$	14160.01	11819.85	15749.80	11285.49	13874.46	12846.66	8.00%
$4f_2 5d$	$^2L_{11/2}$	$(4, 3/2)_{11/2}$	12614.12	14073.38	11151.44	12656.52	13740.95	13352.10	2.91%
$4f_3$	$^2D_{7/2}$	$(7/2)_{7/2}$	14885.84	12501.43	15249.68	13407.63	12854.25	13887.60	7.44%
$4f_3$	$^4D_{5/2}$	$(5/2)_{5/2}$	16882.02	15466.66	12763.88	15297.72	13752.29	14187.35	3.07%
$4f_2 5d$	$^2I_{9/2}$	$(4, 5/2)_{9/2}$	15542.58	15029.91	11954.67	11907.78	15121.47	14558.82	3.86%
$4f_2 5d$	$^2F_{11/2}$	$(5, 11/2)_{11/2}$	14874.72	16998.92	14070.40	16619.43	15099.27	14859.96	1.61%
$4f_2 5d$	$^2K_{5/2}$	$(4, 5/2)_{5/2}$	15288.53	17417.69	12580.62	17779.54	15474.70	15045.80	2.85%
$4f_3$	$^2H_{7/2}$	$(7/2)_{7/2}$	17735.69	14016.27	18781.51	15082.44	13650.54	15443.48	11.61%
$4f_2 5d$	$^2L_{13/2}$	$(5, 13/2)_{13/2}$	14299.77	13519.77	13758.01	16407.71	14450.47	15454.16	6.49%
$4f_2 5d$	$^2D_{11/2}$	$(4, 11/2)_{11/2}$	16863.21	17168.58	12301.18	13995.94	17088.29	15525.50	10.07%

C. Er II and Er III

1. Available data

Extensive research has been conducted on the energy levels and spectral characteristics of singly ionised erbium (Er II), with many studies advancing the understanding of its configurations and transitions. McNally & Sluis (1959) [74] detailed eight low-lying levels of the $4f^{12} 6s$ configuration, drawing on Zeeman data from Lindner & Davis (1958) [75] and wavelength measurements from Gatterer & Junkes (1945) [76]. These levels were further categorised into four Jj terms by Judd & Marquet (1962) [77], who observed that the spacings between components were affected by the Coulomb interaction between the $6s$ electron and the $4f^{12}$ core.

Building on this work, Goldschmidt (1963) [78] computed all 24 levels of the $4f^{12} 6s$ configuration by fitting the F_{2n} Slater parameters using the initial eight experimentally determined levels as a reference. Subsequently, Marquet & Davis (1965) [79] identified 10 levels of the ground configuration using wavelengths in the visible and near-ultraviolet regions. Their Zeeman structure measurements of 132 transitions enabled Sluis & McNally (1970) [80] to identify 12 of the lowest ground configuration levels, which exhibited slightly higher energies than those calculated by Goldschmidt (1963) with $E^2 = 30$.

Additionally, Sluis & McNally (1970) reported 90 odd levels, but these were excluded from comparisons due to a lack of configuration identification and J assignment.

Spector (1971) [81] examined infrared photography from electrodeless discharge and sliding spark, identifying four levels of the $4f 5d$ configuration, which are included in the NIST database. This analysis encompassed 40 odd levels in the 25000–33000 cm^{-1} energy range. The data from the aforementioned studies, including an unpublished extension of the analysis by van Kleef and Koot (1975), have been compiled and systematised in the Handbook of Basic Atomic Spectroscopic by J. E. Sansonetti and W. C. Martin (2005) [58] and are available in the NIST database.

In more recent work, Wyart & Lawler (2009) [82] expanded the spectrum classification both theoretically and experimentally. Initially, they interpreted known energy levels parametrically using Cowan’s code [41] on two sets of interacting configurations. These predictions extended the classification of hollow-cathode FT spectra of erbium recorded at the US National Solar Observatory on Kitt Peak. Using CI, they assigned all 130 known levels of even parity to the $4f^{12}\{6s, 5d\}$ and $4f^{11}\{6s6p, 5d6p\}$ configurations, and 230 known levels of odd parity to the $4f^{12} 6p$ and $4f^{11}\{5d6s, 5d^2, 6s^2\}$ configurations. They also introduced 32 new energy levels and revised the J -values for six levels.

Research into the energy levels and spectral character-

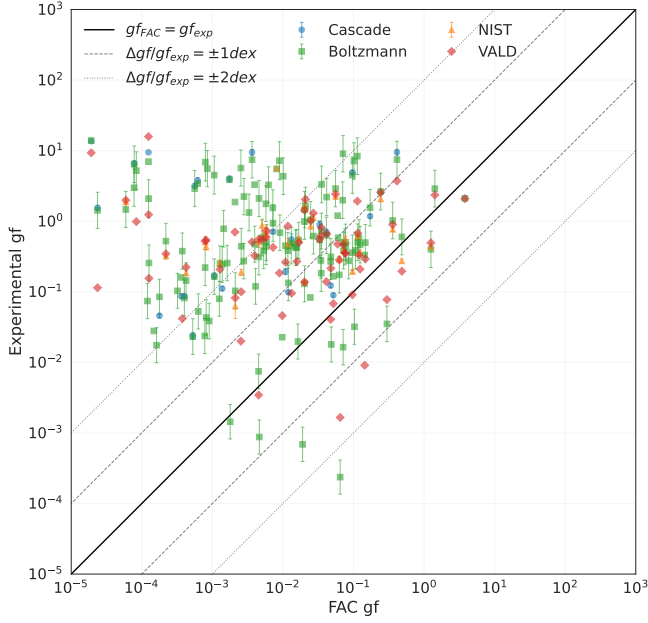


FIG. 7. Comparison of calculated $\log(gf)$ values from *CIS3* model with experimental data for Pr II. The y-axis shows the experimental $\log(gf)$ values, while the x-axis represents the calculated values. Different colours indicate the source of the experimental data: cascade (blue circles), Boltzmann plot method (green squares), VALD (red squares) and the NIST database (orange triangles).

istics of doubly ionised erbium (Er III) has identified both even and odd configurations. For even configurations, the identified levels include $4f^{12}$ and $4f^{11}6p$, while odd configurations are $4f^{11}6s$ and $4f^{11}5d$.

Becher (1966) [83] was one of the first to analyse its spectrum by identifying nine levels within the $4f^{11}(4f_{15/2})5d$, $4f^{11}(4f_{15/2})6s$, and $4f^{11}(4f_{15/2})6p$ groups. He noted the J_1j coupling in these sub-configurations and assigned levels to all five J_1j terms based on the $4f^{11}(4f_{15/2})$ parent level.

Most of the levels and term assignments were further detailed by Spector (1973) [84], who independently found a more comprehensive system of excited levels and positioned them relative to three levels of the $4f^{12}$ ground configuration, including the ground level. Wyart, Blaise, and Camus (1974) [64] studied the $(4f^{11}5d + 4f^{11}6s)$ configurations for Er III, adding two levels and suggesting the removal of two others from Spector’s list. They also calculated the leading percentages in LS coupling from their paper, noting that three of these levels could not be unambiguously assigned to calculated eigenvectors.

Wyart, Koot, and van Kleef (1974) [85] further calculated the percentages in J_1j coupling for the $4f^{11}6p$ group of levels and identified two new levels of $4f^{11}5d$. Lastly, the data from Becher were reanalyzed by Wyart et al. (1997) [86] increasing the number of identified levels from 45 to 115.

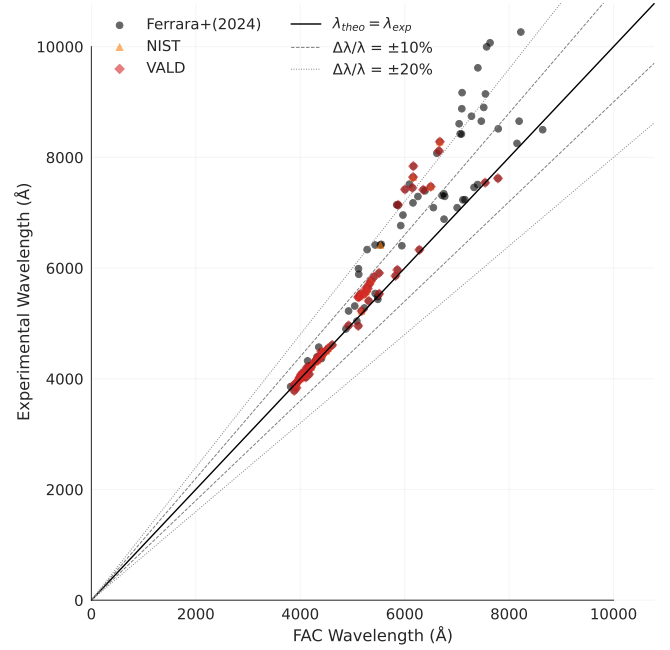


FIG. 8. Evaluation of calculated wavelengths from *CIS3* model with experimental data for Pr II. The y-axis shows the experimental wavelengths in Angstroms, while the x-axis represents the calculated wavelengths. Grey dots represent comparison to available experimental data from Ferrara et al. (2024) [72], while orange triangles and red squares compare our data with data available in VALD and NIST ASD, respectively. The dashed lines indicate a 10% difference from the experimental data, while the dotted lines show a 20% difference.

2. Computational Procedure

The computational procedure for Er II and Er III followed a similar approach to that used for Pr II and Pr III. The first stage involved determining the fictitious mean configuration (FMC) to establish the optimal potential, using a reference dataset that included several accurately determined low-lying levels. The NIST ASD served as the main reference for constructing this dataset.

The basis space for Er II and Er III was expanded to include all major configurations up to the ionisation energy. SD excitations from the ground configuration ($4f^{12}6s$ for Er II and $4f^{12}$ for Er III) up to $\{7s, 7p, 7d, 5f, 5g\}$ were considered. This space was once again designated as the Optimisation Space (OPS) in the optimisation procedure to determine the optimal FMC.

Due to computational constraints, excitations were included up to CIS2. No core-core or core-valence correlations were included. The configuration space was expanded as follows:

- OPS = GC + SD $\{7s, 7p, 7d, 5f, 5g\}$
- CIS1 = OPS + SD $\{8s, 8p, 8d, 6f, 5g\}$
- CIS2 = CIS1 + SD $\{9s, 9p, 9d, 7f, 6g\}$

3. Energy Levels

The energy levels calculated for Er II and Er III have been rigorously compared with the recommended values of the NIST database, as shown in Fig. 9 and Fig. 10. Similarly to the results observed for Pr II and Pr III, the initial calculations using a configuration set equivalent to OPS reveal significant discrepancies from the NIST data. However, when FMC optimisation is applied, a notable enhancement in accuracy is achieved. Detailed results for the first few levels are shown in Tables III and IV.

In Fig. 9, the optimised results for lower energy levels align closely with the NIST data, showing the effectiveness of the FMC optimisation. However, for higher energy levels, although there is improvement, discrepancies persist. This is particularly noticeable in the even parity levels, where the optimised results still show some deviations from the NIST data. In general, such discrepancies can create imbalances in the optimisation process, potentially leading to issues like overfitting, especially in odd levels. Including more configurations in the CI usually mitigates these discrepancies. Furthermore, the absence of the lowest levels for $J = 3, 5$ and 7 for odd parity in the NIST database reduces the reliability of the comparisons for those levels.

In Fig. 10, the optimised results show that the level density is a much better match to the NIST data compared to the non-optimised case. This indicates that not only are individual levels shifted closer to the reference values but also the overall spectral density improves significantly with optimisation, even though only a few levels are found for even parity. However, it is important to note that this optimisation is highly dependent on the available data. Should missing levels be discovered in the range $0\text{-}60000\text{ cm}^{-1}$ for even parity, the results may become inaccurate, necessitating the determination of a new FMC.

The relative differences between our calculated energy levels and the NIST data for Er II and Er III across different computational models are depicted in Fig. 11. The "No Opt." model, representing the OPS configuration without FAC potential optimisation, shows higher relative differences compared to models that include this optimisation. The optimisation leads to a substantial reduction in relative differences, outperforming the use of just CI, as was also evident in the results for Pr II and Pr III. Moreover, examining the progression across different CI spaces (CIS1 and CIS2) shows that the optimisation maintains consistent improvements in accuracy, demonstrating the robustness of our approach.

4. Transitions

To gauge the reliability of our results for Er II, we again utilized the extensive experimental data from Ferrara et al. 2024 and available data from VALD and NIST ASD. Fig. 12 illustrates the comparison between $\log(gf)$ val-

ues calculated using our CIS2 model and the experimental data for Er II. As with the praseodymium data, the experimental values were obtained through both Boltzmann plots and using a cascade method.

As evident from Fig. 12, there is significant scatter in the $\log(gf)$ values throughout the range of transition strengths. The agreement between our calculations and the experimental data does not show a clear trend with transition strength, unlike what was observed for Pr II. Quantitatively, we observe a RMSD of approximately 1.4 dex between our calculated $\log(gf)$ values and the experimental data. This level of disagreement is comparable to what we found for Pr II.

In contrast, Fig. 13 demonstrates excellent agreement between our calculated wavelengths and the experimental values for Er II. Most of the calculated wavelengths fall well within 10% of the experimental data, as indicated by the points that lie between the inner dotted lines. Virtually all calculated wavelengths are within 20% of the experimental values, falling between the dashed lines. Quantitatively, we find that approximately 85% of our calculated wavelengths deviate by less than 10% from the experimental values, and over 95% are within 20%.

The stark contrast in accuracy between the transition probabilities and the wavelengths observed for Er II mirrors our findings for Pr II. This discrepancy can be attributed to the nature of our optimisation procedure, which is primarily designed to minimise differences in energy levels when compared to experimental data. While this approach typically leads to more accurate wavefunctions, these results clearly demonstrate its limitations. The high accuracy in wavelength predictions, which are primarily determined by energy level differences, is a direct consequence of this optimisation strategy. However, persistent discrepancies in oscillator strengths suggest that our current approach may not fully capture the intricacies of the wavefunctions required for accurate transition probability calculations. This indicates that including a larger basis set in our calculations may be necessary to improve the accuracy of oscillator strengths, as these are more sensitive to the fine details of the electronic wavefunctions.

V. SYSTEMATIC CALCULATIONS

With the aid of the optimisation technique described earlier, comprehensive calculations for multiple relevant r-process ions were conducted. According to kilonova models generated by radiative transfer codes for times $t_{\text{exp}} \gtrsim 1$ days, we focused on singly and doubly ionised ions due to their significant roles in the line-forming regions [25]. Although higher ionisation stages are relevant at earlier stages and much higher temperatures, the impact of neutral species has been a recent topic of debate within the community. Because of their higher computational expense, calculations for relevant neutral ions are still under development. A notable use case of this opti-

TABLE III. Energy levels (in cm^{-1}) for the first 20 levels of Er II. The columns show: electronic configuration (Config.), level labels in LS and jj coupling, calculated energies without optimization ($E_{\text{no-OPS}}$), with optimization space only (E_{OPS}), and with increasing configuration interaction spaces (E_{CIS1} , E_{CIS2}). The experimental values from NIST (E_{NIST}) and relative differences between CIS2 and experimental values ($\Delta_{\text{CIS2}}(\%)$) are given in the last two columns.

Config.	LSJ	jj	$E_{\text{no-OPS}}$	E_{OPS}	E_{CIS1}	E_{CIS2}	E_{NIST}	$\Delta_{\text{CIS2}}(\%)$
$4f_{12} 6s$	$^4H_{13/2}$	$(6, 1/2)_{13/2}$	16791.28	0.00	0.00	0.00	0.00	—
$4f_{12} 6s$	$^2H_{11/2}$	$(6, 1/2)_{11/2}$	17556.49	515.66	661.75	442.86	440.43	0.65%
$4f_{12} 6s$	2G_4	$(4, 1/2)_{9/2}$	23985.62	5652.03	5774.19	5238.72	5132.61	2.07%
$4f_{12} 6s$	2H_3	$(4, 1/2)_{7/2}$	23057.16	5791.67	6053.75	5495.85	5403.69	1.71%
$4f_{11} 6s^2$	$^4I_{15/2}$	$(15/2)_{15/2}$	6087.28	7190.58	9328.78	9347.81	6824.77	36.96%
$4f_{12} 6s$	$^4H_{11/2}$	$(5, 1/2)_{11/2}$	23944.58	7545.72	10790.22	7434.18	7149.63	3.98%
$4f_{12} 6s$	$^2H_{9/2}$	$(5, 1/2)_{9/2}$	22659.28	8208.46	8493.39	7590.97	7195.35	5.02%
$4f_{11} 5d 6s$	$^4F_{13/2}$	$(15/2, 3/2, 1/2)_{13/2}$	9499.76	11788.31	11845.91	11160.24	10667.19	4.62%
$4f_{12} 6s$	$^2K_{7/2}$	$(4, 1/2)_{7/2}$	27905.85	12532.39	12803.65	11486.81	10893.94	5.56%
$4f_{12} 6s$	$^4F_{9/2}$	$(4, 1/2)_{9/2}$	28110.92	13867.35	13128.59	11615.88	11042.64	5.19%
$4f_{11} 5d 6s$	$^4H_{15/2}$	$(15/2, 3/2, 1/2)_{15/2}$	10886.83	12942.23	14537.95	12035.95	11309.18	6.51%
$4f_{11} 5d 6s$	$^4F_{11/2}$	$(15/2, 3/2, 1/2)_{11/2}$	12837.32	14064.20	14482.92	13194.92	12388.09	6.51%
$4f_{12} 6s$	$^2K_{7/2}$	$(6, 1/2)_{7/2}$	30661.42	13848.06	13338.24	14148.52	12588.00	14.17%
$4f_{12} 6s$	$^4F_{5/2}$	$(6, 1/2)_{5/2}$	30660.60	14923.55	15829.49	14247.63	12600.09	13.09%
$4f_{11} 5d 6s$	$^4F_{19/2}$	$(15/2, 5/2)_{19/2}$	11191.85	15128.19	16687.78	13992.21	12815.07	9.21%
$4f_{11} 5d^2$	$^2F_{17/2}$	$(15/2, 2)_{17/2}$	12529.68	16320.09	13955.52	13921.83	13027.93	7.87%
$4f_{11} 5d^2$	$^4F_{13/2}$	$(15/2, 2)_{13/2}$	13089.82	17160.48	14199.61	15838.63	13060.72	21.28%
$4f_{12} 6s$	$^6H_{3/2}$	$(2, 1/2)_{3/2}$	31496.55	15922.44	14289.71	14762.72	13188.47	11.93%
$4f_{11} 6^2$	$^4I_{13/2}$	$(13/2)_{13/2}$	13951.13	18536.90	15507.67	19659.70	13338.78	47.35%
$4f_{12} 6s$	$^4F_{1/2}$	$(2, 1/2)_{5/2}$	32244.40	18581.69	17380.42	14683.12	13558.33	8.30%

misation technique was highlighted in a previous study, which focused on singly and doubly ionised Nd and U. This optimisation was performed manually using a uniform search grid of 100 values. The chosen FMC was the one that best reproduced the experimental energy of the lowest levels for each J and the parity value [35].

The calculations are performed in two primary stages. First, the FMC, used to determine the optimal potential, is computed using a reference dataset that includes accurately determined low-lying levels. The data from the NIST database was the primary reference for building this dataset [27]. An exception was made for Dy III, for which data from the experimental work of Spector et al. was used as a reference [87]. Tables V and VI summarise the optimisation characteristics and performance for single- and doubly ionised lanthanide ions, respectively. The improvement factors demonstrate the consistent effectiveness of our optimisation approach across the series, with particularly notable improvements for ions with well-characterised electronic structures.

Secondly, the basis space is increased to include all major configurations up to the ionisation energy. For lanthanides, it was found that considering SD excitation from the ground configuration up to $\{8s, 8p, 7d\}$ effectively covers the most relevant configurations that directly contribute to opacity. Additional configurations, based on excitations up to $n = 9$ and $\ell = 4$, were included in the CI basis to improve the convergence of the

results.

Figures 14 and 15 provide a summary of the average precision for single- and doubly ionised lanthanide calculations performed during this work. A difference of around 10%, and in some cases lower, compared to the NIST data was found for both ionisation stages. These results align with, and in some cases improve upon, the systematic calculations performed with the HULLAC code and available in the Japan-Lithuania opacity database for kilonova (2021). Additionally, unlike individual-level calibration, the optimisation of the central potential impacts the entire energy spectrum and, consequently, the level density. Although some differences have been observed compared to *ab initio* calculations using the Hartree-Fock relativistic code (HFR), based on [41], the direct effect on opacity under local thermodynamical equilibrium conditions is expected to be minor, with more significant impacts at energies close to the ionisation energy.

Following the same calculation procedure used for the lanthanides, structure calculations were also performed for all singly- and doubly ionised actinides. In this case, because of the scarcity of actinide data in the NIST database, the reference energy levels for the optimisation of the FMC were sourced from the Selected Constants Energy Levels and Atomic Spectra of Actinides (SCASA) [88], available as an online database. Whenever the number of experimental levels was insufficient for reliable optimisation, a fictitious configuration based

TABLE IV. Energy levels (in cm^{-1}) for the first 20 levels of Er III. The columns show: electronic configuration (Config.), level labels in LS and jj coupling, calculated energies without optimization ($E_{\text{no-OPS}}$), with optimization space only (E_{OPS}), and with increasing configuration interaction spaces (E_{CIS1} , E_{CIS2}). The experimental values from NIST (E_{NIST}) and relative differences between CIS2 and experimental values (Δ_{CIS2}) are given in the last two columns.

Config.	LSJ	jj	$E_{\text{no-OPS}}$	E_{OPS}	E_{CIS1}	E_{CIS2}	E_{NIST}	$\Delta_{\text{CIS2}}(\%)$
$4f_{12}$	3H_6	(6) ₆	8549.20	0.00	0.00	0.00	0.00	—
$4f_{12}$	3F_4	(4) ₄	13986.81	6379.26	6426.10	6187.68	5081.79	21.76%
$4f_{12}$	3H_5	(5) ₅	15452.62	7607.98	7734.53	6306.63	6969.78	9.51%
$4f_{12}$	3H_4	(4) ₄	19390.33	11699.33	12083.23	10558.93	10785.48	2.10%
$4f_{11} 5d$	3F_6	(15/2, 3/2) ₆	18680.31	19945.03	19118.33	14071.95	16976.09	17.11%
$4f_{11} 5d$	1D_7	(15/2, 3/2) ₇	13700.74	20431.81	19052.84	15053.80	17647.76	14.70%
$4f_{11} 5d$	5H_9	(15/2, 3/2) ₉	16825.73	21728.27	19570.55	19060.32	18976.74	0.44%
$4f_{11} 5d$	3P_8	(15/2, 3/2) ₈	18330.78	21319.04	19606.51	17325.56	19315.90	10.30%
$4f_{11} 5d$	5K_8	(15/2, 3/2) ₈	21683.07	23223.31	22518.24	20539.81	19918.17	3.12%
$4f_{11} 5d$	3H_7	(15/2, 3/2) ₇	19491.41	22174.29	22707.52	21519.74	20226.20	6.40%
$4f_{11} 5d$	${}^3P_{10}$	(15/2, 5/2) ₁₀	15098.56	17639.37	18084.44	17200.91	20470.13	15.97%
$4f_{11} 5d$	3H_9	(15/2, 5/2) ₉	22969.92	26168.92	26496.96	25397.46	21688.17	17.10%
$4f_{11} 5d$	3K_5	(15/2, 5/2) ₅	22888.83	21061.99	24145.93	19851.71	22016.77	9.83%
$4f_{11} 5d$	5I_6	(15/2, 5/2) ₆	23823.06	21723.57	23138.71	20662.19	22606.07	8.60%
$4f_{11} 6s$	3I_8	(15/2, 5/2) ₈	24388.94	24292.88	23495.02	23135.29	22951.42	0.80%
$4f_{11} 6s$	5K_7	(15/2, 5/2) ₇	23044.05	20474.16	20383.00	24433.67	23302.78	4.85%
$4f_{11} 5d$	3I_8	(13/2, 3/2) ₈	27084.63	23071.16	24660.08	26950.80	25482.12	5.76%
$4f_{11} 5d$	5K_7	(13/2, 1/2) ₇	25501.29	29257.19	24928.37	25305.76	26102.80	3.05%
$4f_{11} 5d$	5K_5	(15/2, 3/2) ₅	25940.92	26752.22	27523.70	25187.40	26192.66	3.84%
$4f_{11} 5d$	5I_6	(13/2, 1/2) ₆	26115.01	25562.72	23877.65	26226.36	26411.80	0.70%

TABLE V. Summary of optimization characteristics for singly ionized lanthanide ions. For each ion we list: the number of experimental levels used as reference data (N_{ref}), number of iterations required for convergence (N_{iter}), root mean square deviation (RMSD) between calculated and experimental energy levels before and after optimization. The reference data is taken from the NIST ASD. The improvement factor indicates the ratio of initial to final RMSD.

Ion	N_{ref}	N_{iter}	$\text{RMS}_{\text{initial}} (\text{cm}^{-1})$	$\text{RMS}_{\text{final}} (\text{cm}^{-1})$	Improvement factor
La II	42	52	1418	673	2.11
Ce II	86	47	2384	1122	2.13
Pr II	97	54	3005	1601	1.88
Nd II	156	60	1552	1159	1.34
Pm II	38	48	5447	1276	4.27
Sm II	122	51	1304	1024	1.27
Eu II	89	50	4514	1422	3.17
Gd II	239	117	2598	1770	1.47
Tb II	72	103	6602	1200	5.50
Dy II	245	95	4141	706	5.87
Ho II	43	112	6219	1341	4.64
Er II	156	106	2092	1643	1.27
Tm II	168	124	2902	844	3.44
Yb II	142	67	3733	1767	2.11

on the FMC of the homologous lanthanide ion was constructed. The results and their consequent impact on opacities are currently being analysed, and publications are expected in the near future.

VI. CONCLUSIONS

This study presents a novel approach to optimise atomic structure calculations using the FAC for complex multielectron systems, with a particular focus on

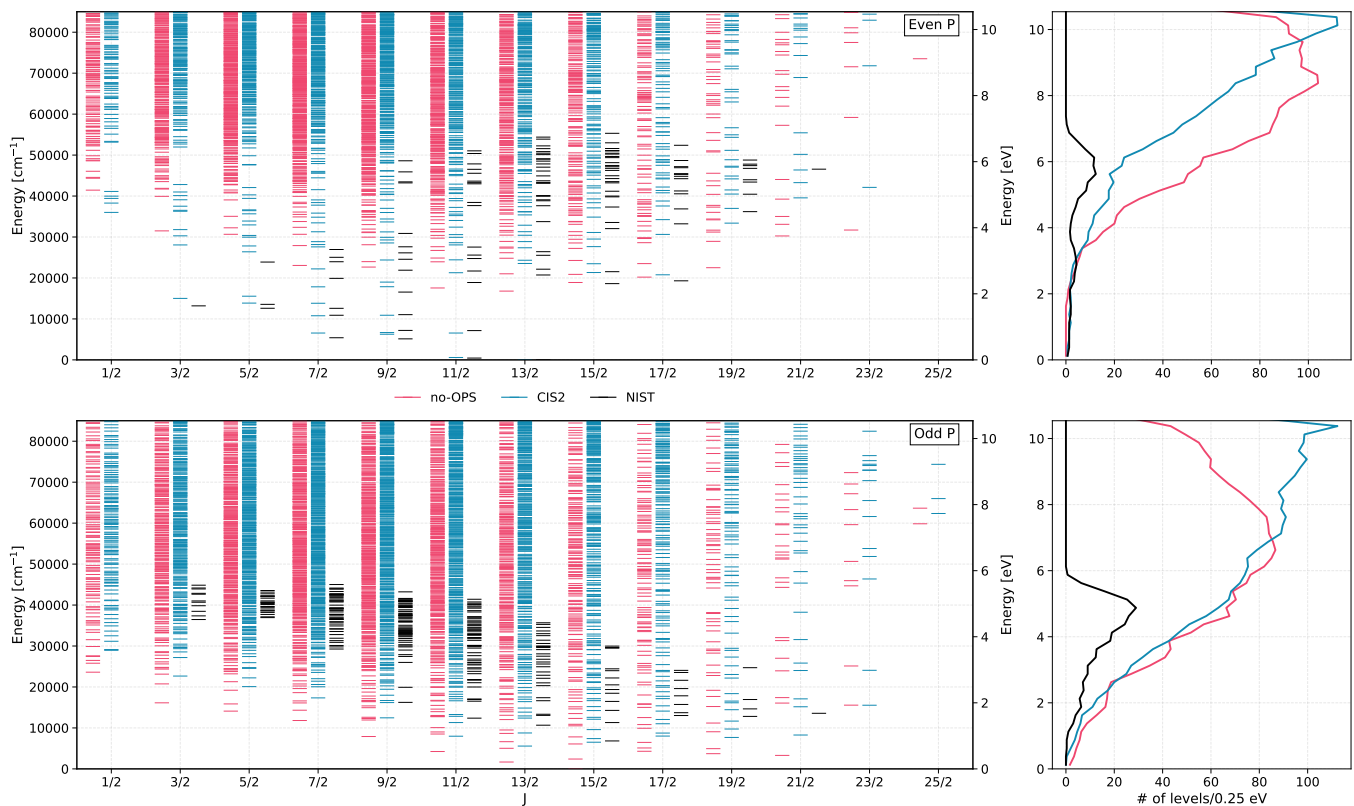


FIG. 9. Energy levels and level density of Er II. Pink lines show results for a calculation without optimisation of the FMC (using a set of configurations equivalent to OPS) while blue lines show the results for our largest calculation, including the optimisation. Black horizontal lines show the data from the NIST ASD [27]

lanthanide and actinide ions relevant to r -process nucleosynthesis and kilonova modelling. Our method, centred on the optimisation of the fictitious mean configuration (FMC), has demonstrated significant improvements in the accuracy of calculated energy levels and transition properties for a range of elements and ionisation states.

The FMC optimisation technique has substantially improved the accuracy of the calculated energy levels for Au II, Pt II, Pr II, Pr III, Er II, and Er III. We observed a notable reduction in the average relative difference from NIST data, typically 20-60% in unoptimized calculations to less than 10% with our optimised approach. This improvement is particularly noteworthy for low-lying energy levels, which are crucial for accurate spectroscopic modelling.

Our optimised method has shown exceptional performance in calculating transition wavelengths. For both Pr and Er ions around 85-90% of our calculated wavelengths fall within 10% of experimental measurements. This high level of accuracy is essential for reliable identification and analysis of spectral features in astrophysical observations, particularly in the context of kilonova spectra. While we observed significant improvements in energy level calculations and wavelength predictions, the computation of transition probabilities ($\log(gf)$ values) remains challenging. Although our optimised calcula-

tions show improvement compared to unoptimized results, notable discrepancies persist. These discrepancies highlight the inherent difficulties in accurately representing electron correlations in complex ionic systems, especially for lanthanides and actinides with open f -shells.

The effectiveness of our optimisation procedure across the lanthanide series demonstrates its broad applicability to elements with varying $4f$ shell complexities. This versatility is crucial for comprehensive modelling of r -process nucleosynthesis, where a wide range of elements play important roles. Our systematic calculations for singly and doubly ionised lanthanides have achieved accuracies comparable to, and in some cases better than, those obtained with other widely used codes like HULLAC, as evidenced by comparisons with the Japan-Lithuania opacity database for kilonova.

The success of this optimisation technique in improving the accuracy of atomic structure calculations has important implications for astrophysical modelling, particularly in the context of kilonova spectra and r -process nucleosynthesis. By providing more accurate atomic data, our work contributes to enhancing the reliability of opacity calculations and spectral modelling for heavy elements in extreme astrophysical environments. This improved accuracy is critical for interpreting observational data from kilonova events and understanding the produc-

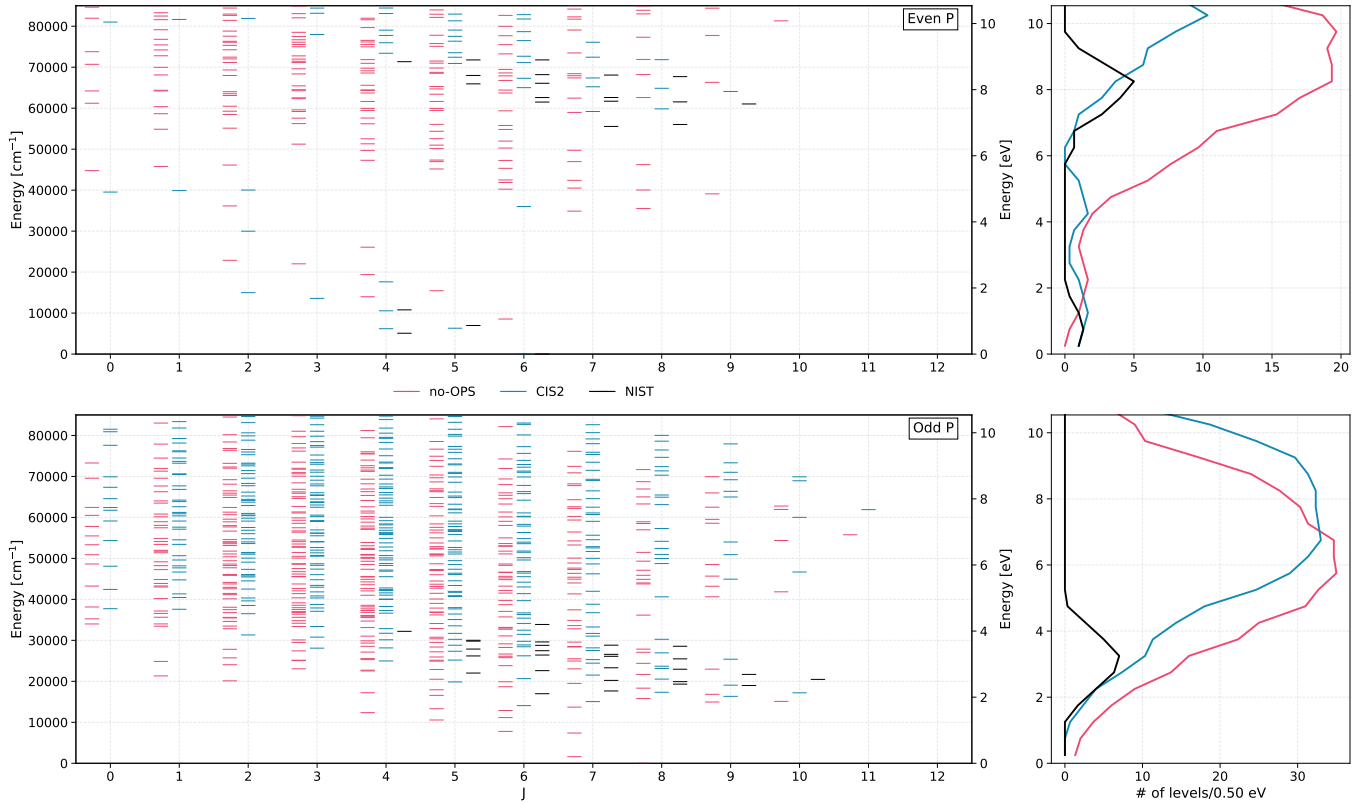


FIG. 10. Energy levels and level density of Er III. Pink lines show results for a calculation without optimisation of the FMC (using a set of configurations equivalent to OPS) while blue lines show the results for our largest calculation, including the optimisation. Black horizontal lines show the data from the NIST ASD.[27]

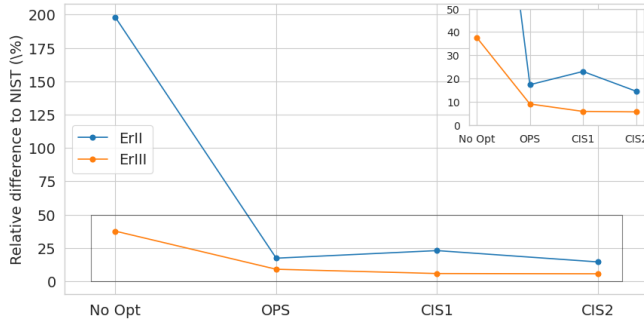


FIG. 11. Average relative difference to the data available in the NIST ASD [27] for all identified levels of Er II and Er III for all the different models computed with FAC. “No Opt.” corresponds to an OPS configuration model that does not use the FAC potential optimisation, contrary to the other models.

tion and distribution of heavy elements in the universe.

However, persistent challenges in calculating accurate transition probabilities underscore the need for further refinement of our approach. Future work should focus on expanding the basis set to potentially improve the accuracy of oscillator strengths and transition probabilities. Although computationally demanding, investigating the inclusion of core-core and core-valence correlations may

further enhance the accuracy of energy level and transition calculations. The demonstrated success of our optimisation approach in improving energy level calculations is particularly valuable as it enables more reliable level identification. This enhanced identification capability provides a solid foundation for future work involving detailed calibration of theoretical energy levels against experimental data [89].

Extending the optimisation technique to neutral species and higher ionisation stages is another important avenue for future research. This extension would allow for coverage of a broader range of astrophysical conditions, from the early, hot phases of kilonova evolution to later, cooler stages where lower ionisation states become relevant. Furthermore, applying this method to a wider range of elements, particularly actinides, will support a more comprehensive modelling of r -process nucleosynthesis.

ACKNOWLEDGEMENTS

RFS acknowledges the support from National funding by FCT (Portugal), through the individual research grant 2022.10009.BD. RFS, JMS, and JPM acknowledge the support from FCT (Portugal) through

TABLE VI. Summary of optimization characteristics for doubly ionized lanthanide ions. For each ion we list: the number of experimental levels used as reference data (N_{ref}), number of iterations required for convergence (N_{iter}), root mean square deviation (RMSD) between calculated and experimental energy levels before and after optimization. The reference data is taken from the NIST ASD, except for Dy III, where the data is sourced from Spector et al (1997) [87]. No reliable experimental data for energy levels was found for Pm III besides for the ground state. The improvement factor indicates the ratio of initial to final RMSD.

Ion	N_{ref}	N_{iter}	$\text{RMSD}_{\text{initial}} (\text{cm}^{-1})$	$\text{RMSD}_{\text{final}} (\text{cm}^{-1})$	Improvement factor
La III	41	19	3200	1485	2.15
Ce III	224	34	5591	1482	3.77
Pr III	389	38	2717	1707	1.59
Nd III	30	22	2233	1895	1.18
Pm III	1	32	1690	1667	1.01
Sm III	58	25	9119	2814	3.24
Eu III	118	71	6254	1259	4.96
Gd III	258	68	11556	1876	6.16
Tb III	111	89	4653	4575	1.02
Dy III	107	91	5828	2647	2.20
Ho III	48	33	12601	1881	6.70
Er III	53	26	2360	1640	1.44
Tm III	129	29	1974	1513	1.31
Yb III	55	24	1459	678	2.15

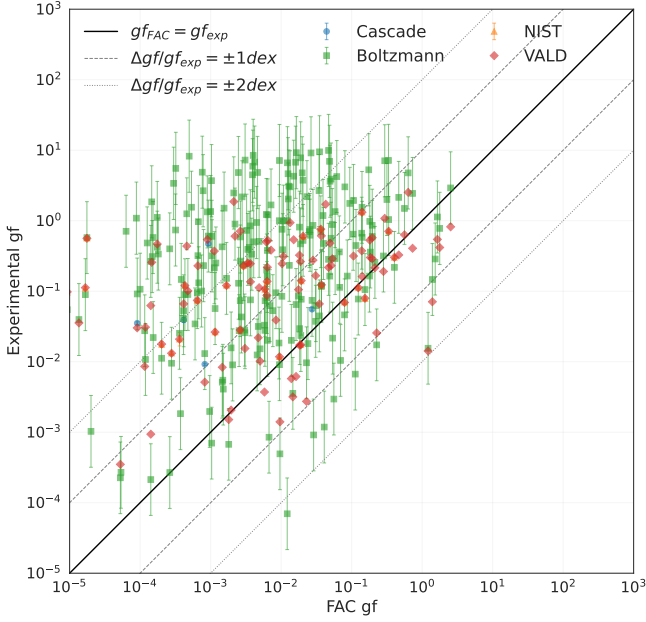


FIG. 12. Comparison of calculated $\log(gf)$ values from CIS2 model with experimental data for Er II. The y-axis shows the experimental $\log(gf)$ values, while the x-axis represents the calculated values. Different colours indicate the source of the experimental data: cascade (blue circles), Boltzmann plot method (green squares), VALD (red squares) and the NIST database (orange triangles).

research center fundings UIDP/50007/2020 (LIP) and UID/04559/2020 (LIBPhys), through project funding 2022.06730.PTDC, "Atomic inputs for kilonovae model-

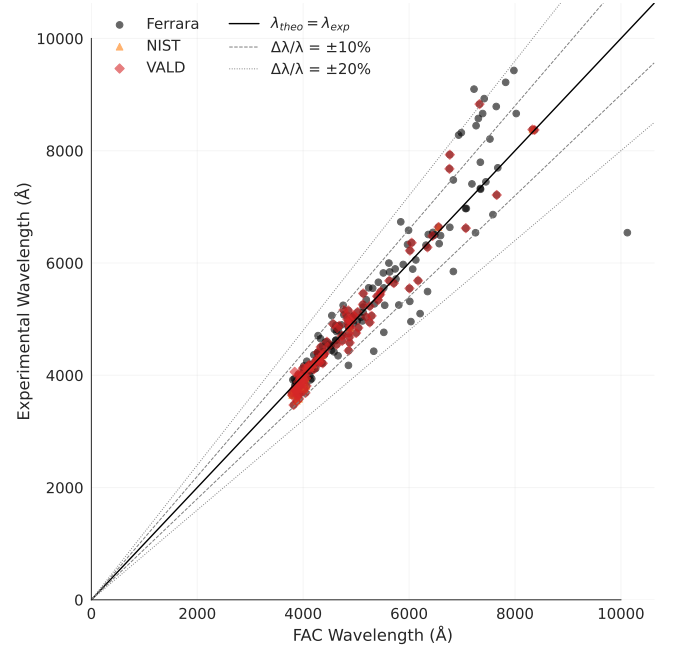


FIG. 13. Comparison of calculated wavelengths from CIS2 model with experimental data for Er II. The y-axis shows the experimental wavelengths in Ångstroms, while the x-axis represents the calculated wavelengths. Grey dots represent comparison to available experimental data from Ferrara et al. (2024) [72], while orange triangles and red squares compare our data with data available in VALD and NIST ASD, respectively. The dashed lines indicate a 10% difference from the experimental data, while the dotted lines show a 20% difference.

ing (ATOMIK)” and, partly through project funding 2023.14470.PEX ”Spectral Analysis and Radiative Data for Elemental Kilonovae Identification (SPARKLE) [90]”. GMP and AF acknowledge support by the European Research Council (ERC) under the European Union’s Horizon 2020 research and innovation programme (ERC Advanced Grant KILONOVA No. 885281), the Deutsche

Forschungsgemeinschaft (DFG, German Research Foundation) - Project-ID 279384907 - SFB 1245, and MA 4248/3-1, and the State of Hesse within the Cluster Project ELEMENTS.

This work has made use of the VALD database, operated at Uppsala University, the Institute of Astronomy RAS in Moscow, and the University of Vienna.

-
- [1] J. M. Lattimer and D. N. Schramm, Black-hole-neutron-star collisions, *Astrophys. J.* **192**, L145 (1974).
- [2] J. M. Lattimer and D. N. Schramm, The tidal disruption of neutron stars by black holes in close binaries, *Astrophys. J.* **210**, 549 (1976).
- [3] D. Eichler, M. Livio, T. Piran, and D. N. Schramm, Nucleosynthesis, neutrino bursts and γ -rays from coalescing neutron stars, *Nature* **340**, 126 (1989).
- [4] S. Rosswog, M. Liebendörfer, F.-K. Thielemann, M. B. Davies, W. Benz, and T. Piran, Mass ejection in neutron star mergers, *Åpent rom* **341**, 499 (1999).
- [5] C. Freiburghaus, S. Rosswog, and F. Thielemann, R-process in neutron star mergers, *Astrophys. J.* **525**, L121 (1999).
- [6] B. D. Metzger, G. Martínez-Pinedo, S. Darbha, E. Quataert, A. Arcones, D. Kasen, R. Thomas, P. Nugent, I. V. Panov, and N. T. Zinner, Electromagnetic counterparts of compact object mergers powered by the radioactive decay of r-process nuclei, *Mon. Not. Roy. Ast. Soc.* **406**, 2650 (2010).
- [7] LIGO Scientific Collaboration and Virgo Collaboration *et al.*, Multi-messenger observations of a binary neutron star merger*, *Astrophys. J. Lett.* **848**, L12 (2017).
- [8] P. S. Cowperthwaite *et al.*, The electromagnetic counterpart of the binary neutron star merger LIGO/Virgo GW170817. II. UV, optical, and near-infrared light curves and comparison to kilonova models, *Astrophys. J. Lett.* **848**, L17 (2017).
- [9] D. Kasen, B. Metzger, J. Barnes, E. Quataert, and E. Ramirez-Ruiz, Origin of the heavy elements in binary neutron-star mergers from a gravitational-wave event, *Nature* **551**, 80 (2017).
- [10] S. J. Smartt, Chen, *et al.*, A kilonova as the electromagnetic counterpart to a gravitational-wave source, *Nature* **551**, 75 (2017).
- [11] V. A. Villar, J. Guillochon, E. Berger, B. D. Metzger, P. S. Cowperthwaite, M. Nicholl, K. D. Alexander, P. K. Blanchard, R. Chornock, T. Eftekhari, W. Fong, R. Margutti, and P. K. G. Williams, The combined ultraviolet, optical, and near-infrared light curves of the kilonova associated with the binary neutron star merger GW170817: Unified data set, analytic models, and physical implications, *Astrophys. J. Lett.* **851**, L21 (2017).
- [12] M. Tanaka, D. Kato, G. Gaigalas, P. Rynkun, L. Radziūtė, S. Wanajo, Y. Sekiguchi, N. Nakamura, H. Tanuma, I. Murakami, and H. A. Sakaue, Properties of kilonovae from dynamical and post-merger ejecta of neutron star mergers, *Astrophys. J.* **852**, 109 (2018).
- [13] R. T. Wollaeger, O. Korobkin, C. J. Fontes, S. K. Rosswog, W. P. Even, C. L. Fryer, J. Sollerman, A. L. Hungerford, D. R. van Rossum, and A. B. Wollaber, Impact of ejecta morphology and composition on the electromagnetic signatures of neutron star mergers, *Mon. Not. R. Astron. Soc.* **478**, 3298 (2018).
- [14] M. Bulla, S. Covino, K. Kyutoku, M. Tanaka, J. R. Maund, F. Patat, K. Toma, K. Wiersema, J. Bruten, Z. P. Jin, and V. Testa, The origin of polarization in kilonovae and the case of the gravitational-wave counterpart AT 2017gfo, *Nat. Astron.* **3**, 99 (2018).
- [15] D. Watson, C. J. Hansen, J. Selsing, A. Koch, D. B. Malesani, A. C. Andersen, J. P. U. Fynbo, A. Arcones, A. Bauswein, S. Covino, A. Grado, K. E. Heintz, L. Hunt, C. Kouveliotou, G. Leloudas, A. J. Levan, P. Mazzali, and E. Pian, Identification of strontium in the merger of two neutron stars, *Nature* **574**, 497 (2019).
- [16] K. Kawaguchi, S. Fujibayashi, M. Shibata, M. Tanaka, and S. Wanajo, A low-mass binary neutron star: Long-term ejecta evolution and kilonovae with weak blue emission, *Astrophys. J.* **913**, 100 (2021).
- [17] N. Domoto, M. Tanaka, S. Wanajo, and K. Kawaguchi, Signatures of r-process Elements in Kilonova Spectra, *Astrophys. J.* **913**, 26 (2021).
- [18] J. H. Gillanders, M. McCann, S. A. Sim, S. J. Smartt, and C. P. Ballance, Constraints on the presence of platinum and gold in the spectra of the kilonova AT2017gfo, *Mon. Not. R. Astron. Soc.* **506**, 3560 (2021).
- [19] N. Domoto, M. Tanaka, D. Kato, K. Kawaguchi, K. Hotokezaka, and S. Wanajo, Lanthanide features in near-infrared spectra of kilonovae, *Astrophys. J.* **939**, 8 (2022).
- [20] J. H. Gillanders, S. J. Smartt, S. A. Sim, A. Bauswein, and S. Goriely, Modelling the spectra of the kilonova AT2017gfo – I. The photospheric epochs, *Mon. Not. R. Astron. Soc.* **515**, 631 (2022).
- [21] K. Hotokezaka, M. Tanaka, D. Kato, and G. Gaigalas, Tellurium emission line in kilonova AT 2017gfo, *Mon. Not. R. Astron. Soc. Lett.* **526**, L155 (2023).
- [22] A. Sneppen and D. Watson, Discovery of a 760 nm P Cygni line in AT2017gfo: Identification of yttrium in the kilonova photosphere, *Astron. Astrophys.* **675**, A194 (2023).
- [23] Y. Tarumi, K. Hotokezaka, N. Domoto, and M. Tanaka, Non-LTE analysis for Helium and Strontium lines in the kilonova AT2017gfo, *arXiv [astro-ph.HE]*, arXiv:2302.13061 (2023).
- [24] D. Kasen, N. R. Badnell, and J. Barnes, OPACITIES AND SPECTRA OF THE r-PROCESS EJECTA FROM NEUTRON STAR MERGERS, *Astrophys. J.* **774**, 25 (2013).
- [25] L. J. Shingles, C. E. Collins, V. Vijayan, A. Flörs, O. Just, G. Leck, Z. Xiong, A. Bauswein, G. Martínez-Pinedo, and S. A. Sim, Self-consistent 3D radiative transfer for kilonovae: Directional spectra from merger simulations, *Astrophys. J. Lett.* **954**, L41 (2023).
- [26] S. Fritzsche, Level structure and properties of open f-shell

- elements, *Atoms* **10**, 7 (2022).
- [27] A. Kramida, Yu. Ralchenko, J. Reader, and NIST ASD Team, *NIST Atomic Spectra Database (ver. 5.9)* (2021).
- [28] M. Tanaka, D. Kato, G. Gaigalas, and K. Kawaguchi, Systematic opacity calculations for kilonovae, *Mon. Not. R. Astron. Soc.* **496**, 1369 (2020).
- [29] C. J. Fontes, C. L. Fryer, A. L. Hungerford, R. T. Wollaeger, and O. Korobkin, A line-binned treatment of opacities for the spectra and light curves from neutron star mergers, *Mon. Not. R. Astron. Soc.* **493**, 4143 (2020).
- [30] L. Radziūtė, G. Gaigalas, D. Kato, P. Rynkun, and M. Tanaka, Extended calculations of energy levels and transition rates for singly ionized lanthanide elements. I. pr–Gd, *Astrophys. J. Suppl. Ser.* **248**, 17 (2020).
- [31] L. Radziūtė, G. Gaigalas, D. Kato, P. Rynkun, and M. Tanaka, Extended calculations of energy levels and transition rates for singly ionized lanthanide elements. II. Tb–Yb, *Astrophys. J. Suppl. Ser.* **257**, 29 (2021).
- [32] R. F. Silva, J. M. Sampaio, P. Amaro, A. Flörs, G. Martínez-Pinedo, and J. P. Marques, Structure calculations in Nd III and U III relevant for kilonovae modelling, *Atoms* **10**, 18 (2022).
- [33] C. J. Fontes, C. L. Fryer, R. T. Wollaeger, M. R. Mumpower, and T. M. Sprouse, Actinide opacities for modelling the spectra and light curves of kilonovae, *Mon. Not. R. Astron. Soc.* **519**, 2862 (2022).
- [34] Q. Pognan, A. Jerkstrand, and J. Grumer, NLTE effects on kilonova expansion opacities, *Mon. Not. R. Astron. Soc.* [10.1093/mnras/stac1253](https://doi.org/10.1093/mnras/stac1253) (2022).
- [35] A. Flörs, R. F. Silva, J. Deprince, H. C. Gallego, G. Leck, L. J. Shingles, G. Martínez-Pinedo, J. M. Sampaio, P. Amaro, J. P. Marques, S. Goriely, P. Quinet, P. Palmeri, and M. Godefroid, Opacities of singly and doubly ionised neodymium and uranium for kilonova emission modeling, *Mon. Not. R. Astron. Soc.* **524**, 3083 (2023).
- [36] M. McCann, L. P. Mulholland, Z. Xiong, C. A. Ramsbottom, C. P. Ballance, O. Just, A. Bauswein, G. Martínez-Pinedo, F. McNeill, and S. A. Sim, Luminosity predictions for the first three ionisation stages of W, Pt and Au to probe potential sources of emission in kilonova, arXiv e-prints (2024).
- [37] Q. Pognan, M.-R. Wu, G. Martínez-Pinedo, R. F. da Silva, A. Jerkstrand, J. Grumer, and A. Flörs, Actinide signatures in low electron fraction kilonova ejecta, arXiv e-prints (2024).
- [38] C. Froese Fischer, G. Gaigalas, P. Jönsson, and J. Bieroń, GRASP2018—A FORTRAN 95 version of the general relativistic atomic structure package, *Comput. Phys. Commun.* **237**, 184 (2019).
- [39] P. I. O. Gorceix, J. P. Desclaux, A. Flörs, and R. Ferreira da Silva, MCDF studies of two electron ions I: Electron-electron interaction, *J. Phys. B*, 639 (1987).
- [40] N. R. Badnell, AUTOSTRUCTURE: General program for calculation of atomic and ionic properties, Astrophysics Source Code Library, record ascl:1612.014 (2016).
- [41] R. D. Cowan, *The theory of atomic structure and spectra*, Los Alamos Series in Basic and Applied Sciences (Univ of California Press, Berkeley, CA, 1981).
- [42] A. M. P. Mendez, J. I. D. Filippo, S. D. Lopez, and D. M. Mitnik, Bayesian atomic structure calculations for collisional problems, *J. Phys. Conf. Ser.* **1412**, 132027 (2020).
- [43] M. P. A. Mendez, *Optimización de blancos atómicos y moleculares en procesos colisionales*, Ph.D. thesis, Universidad de Buenos Aires. Facultad de Ciencias Exactas y Naturales (2021).
- [44] A. Bar-Shalom, M. Klapisch, and J. Oreg, HULLAC, an integrated computer package for atomic processes in plasmas, *J. Quant. Spectrosc. Radiat. Transf. Radiative Properties of Hot Dense Matter*, **71**, 169 (2001).
- [45] M. F. Gu, The flexible atomic code, *Can. J. Phys.* **86**, 675 (2008).
- [46] T. Head, M. Kumar, H. Nahrstaedt, G. Louppe, and I. Shcherbatyi, [scikit-optimize/scikit-optimize](https://pypi.org/project/scikit-optimize/) (2021).
- [47] L. Chernysheva and V. Yakhontov, Two-program package to calculate the ground and excited state wave functions in the hartree—fock—dirac approximation, *Computer Physics Communications* **119**, 232 (1999).
- [48] N. Badnell and C. Zhang, A FAC potential for autostructure, *Eur. Phys. J. D* [10.1140/epjd/s10053-024-00873-z](https://doi.org/10.1140/epjd/s10053-024-00873-z) (2024).
- [49] R. Latter, Atomic energy levels for the thomas-fermi and thomas-fermi-dirac potential, *Phys. Rev.* **99**, 510 (1955).
- [50] D. H. Sampson, H. L. Zhang, and C. J. Fontes, A fully relativistic approach for calculating atomic data for highly charged ions, *Phys. Rep.* **477**, 111 (2009).
- [51] D. H. Sampson, H. L. Zhang, A. K. Mohanty, and R. E. Clark, A Dirac-Fock-Slater approach to atomic structure for highly charged ions, *Phys. Rev. A Gen. Phys.* **40**, 604 (1989).
- [52] H. L. Zhang, D. H. Sampson, and A. K. Mohanty, Fully relativistic and quasirelativistic distorted-wave methods for calculating collision strengths for highly charged ions, *Phys. Rev. A Gen. Phys.* **40**, 616 (1989).
- [53] M. Hoffman, E. Brochu, and N. de Freitas, Portfolio allocation for bayesian optimization, in *Proceedings of the Twenty-Seventh Conference on Uncertainty in Artificial Intelligence*, UAI’11 (AUAI Press, Arlington, Virginia, USA, 2011) p. 327–336.
- [54] G. Gaigalas, C. F. Fischer, P. Rynkun, and P. Jönsson, Jj2lsj transformation and unique labeling for energy levels, *Atoms* **5**, [10.3390/atoms5010006](https://doi.org/10.3390/atoms5010006) (2017).
- [55] D. Kato, I. Murakami, M. Tanaka, S. Banerjee, G. Gaigalas, L. Radziūtė, and P. Rynkun, Japan-lithuania opacity database for kilonova (2021), <http://dpc.nifs.ac.jp/DB/Opacity-Database/>, (version 1. 0) .
- [56] C. E. Moore, *Atomic energy levels as derived from the analyses of optical spectra :: volume III. 42Mo to 57La, 72Hf to 89Ac*, Tech. Rep. (Gaithersburg, MD, 1971).
- [57] M. Rosberg and J.-F. Wyart, The spectrum of singly ionized gold, Au II, *Phys. Scr.* **55**, 690 (1997).
- [58] J. E. Sansonetti and W. C. Martin, Handbook of Basic Atomic Spectroscopic Data, *Journal of Physical and Chemical Reference Data* **34**, 1559 (2005).
- [59] J. Reader, N. Acquista, and C. J. Sansonetti, Accurate energy levels for singly ionized platinum (Pt II), *J. Opt. Soc. Am. B* **5**, 2106 (1988).
- [60] J. Blaise and J.-F. Wyart, Energy levels of singly-ionized platinum, *J. Res. Natl. Inst. Stand. Technol.* **97**, 217 (1992).
- [61] J.-F. Wyart, J. Blaise, and Y. N. Joshi, Theoretical study of the odd parity levels and transition probabilities in Pt II, *Phys. Scr.* **52**, 535 (1995).
- [62] N. Rosen, G. R. Harrison, and J. R. McNally, Zeeman

- effect data and preliminary classification of the spark spectrum of praseodymium—pr II, *Phys. Rev.* **60**, 722 (1941).
- [63] A. Ginibre, Fine and hyperfine structures of singly ionised praseodymium: II. parametric interpretation of fine and hyperfine structures for the even levels of singly ionised praseodymium, *Phys. Scr.* **39**, 710 (1989).
- [64] J. F. Wyart, J. Blaise, and P. Camus, Progrès Récents dans l'Interprétation des Configurations $4fN(5d+6s)$ des LanthanidesII. Etude Paramétrique des Configurations, *Phys. Scr.* **9**, 325 (1974).
- [65] A. Ginibre, Classified strong lines of singly ionized praseodymium (Pr II) between 2783 and 25,000 cm^{-1} , *At. Data Nucl. Data Tables* **44**, 1 (1990).
- [66] S. Ivarsson, U. Litzén, and G. M. Wahlgren, Accurate Wavelengths, Oscillator Strengths and Hyperfine Structure in Selected Praseodymium Lines of Astrophysical Interest, *Phys. Scr.* **64**, 455 (2001).
- [67] B. Furmann, D. Stefańska, J. Dembczyński, and E. Stachowska, New Levels and Hyperfine Structure Evaluation in Singly Ionized Praseodymium, *Phys. Scr.* **72**, 300 (2005).
- [68] B. Furmann, D. Stefańska, J. Dembczyński, and E. Stachowska, New electron levels and classified lines in Pr II from hyperfine structure measurements, *At. Data Nucl. Data Tables* **93**, 127 (2007).
- [69] N. Akhtar and L. Windholz, Improved energy levels and wavelengths of Pr II from a high-resolution Fourier transform spectrum, *J. Phys. B At. Mol. Opt. Phys.* **45**, 095001 (2012).
- [70] W. C. Martin, R. Zalubas, and L. Hagan, *Atomic Energy Levels - The Rare-Earth Elements* (National Standard Reference Data System, 1978).
- [71] M. S. Safronova, U. I. Safronova, and C. W. Clark, Correlation effects in La, Ce, and lanthanide ions, *Phys. Rev. A* **91**, 1 (2015).
- [72] C. Ferrara, M. Giarrusso, and F. Leone, Experimental atomic data of spectral lines – I. cs, ba, pr, nd, sm, eu, gd, tb, dy, ho, er, tm, yb, lu, hf, re, and os in the 370–1000 nm interval, *Mon. Not. R. Astron. Soc.* **527**, 4440 (2023).
- [73] T. Ryabchikova, Y. Pakhomov, N. Piskunov, H. C. Stempels, U. Heiter, P. S. Barklem, and R. L. Kurucz, A major upgrade of the vald database, *Physica Scripta* (Online) **90**, 10.1088/0031-8949/90/5/054005 (2024).
- [74] J. R. McNally and K. L. Vander Sluis, Preliminary classification of the spectrum of singly ionized erbium (er II), *J. Opt. Soc. Am.* **49**, 200 (1959).
- [75] J. W. Lindner and S. P. Davis, Zeeman effect data for the spectra of erbium*, *J. Opt. Soc. Am., JOSA* **48**, 542 (1958).
- [76] A. Gatterer and J. Junkes, Atlas der restlinien. spektrien der seltenen erden, Laboratorio Astrofisicodella Specola Vaticana (1945).
- [77] B. R. Judd and I. C. Marquet, Energy levels of er ii†, *J. Opt. Soc. Am., JOSA* **52**, 504 (1962).
- [78] Z. B. Goldschmidt, Energy levels of er II, *JOSA* **53**, 594 (1963).
- [79] L. C. Marquet and S. P. Davis, Atomic energy levels of neutral erbium, *JOSA* **55**, 471 (1965).
- [80] K. L. Vander Sluis and J. R. McNally, Recent zeeman results in er II, *J. Opt. Soc. Am., JOSA* **60**, 94 (1970).
- [81] N. Spector, New low even levels of singly ionized erbium (er ii), *Astrophys. J.* **167**, 205 (1971).
- [82] J.-F. Wyart and J. E. Lawler, Theoretical interpretation and new energy levels in er II, *Phys. Scr.* **79**, 045301 (2009).
- [83] B. J., *PhD Thesis*, Ph.D. thesis, Johns Hopkins Univ., Baltimore (1966).
- [84] N. Spector, Level structure of doubly ionized erbium (er iii), *J. Opt. Soc. Am.* **63**, 358 (1973).
- [85] J. F. Wyart, J. J. A. Koot, and T. A. M. Van Kleef, The configuration $4f116p$ in the lanthanide spectra, *Physica* **77**, 159 (1974).
- [86] J.-F. Wyart, J. Blaise, W. P. Bidelman, and C. R. Cowley, Energy levels and transition probabilities in doubly-ionized erbium (er III), *Phys. Scr.* **56**, 446 (1997).
- [87] N. Spector, J. Sugar, and J.-F. Wyart, Analysis of the third spectrum of dysprosium (Dy III), *J. Opt. Soc. Am. B* **14**, 511 (1997).
- [88] J. Blaise and J.-F. Wyart, (1994).
- [89] A. Flörs, R. F. Silva, J. P. Marques, J. M. Sampaio, and G. Martínez-Pinedo, Calibrated lanthanide atomic data for kilonova radiative transfer. i. atomic structure and opacities (2025), in preparation.
- [90] Spectral analysis and radiative data for elemental kilonovae identification (sparkle), <https://doi.org/10.54499/2023.14470.PEX> (2025), this project has received funding from Fundação para a Ciência e a Tecnologia (FCT).

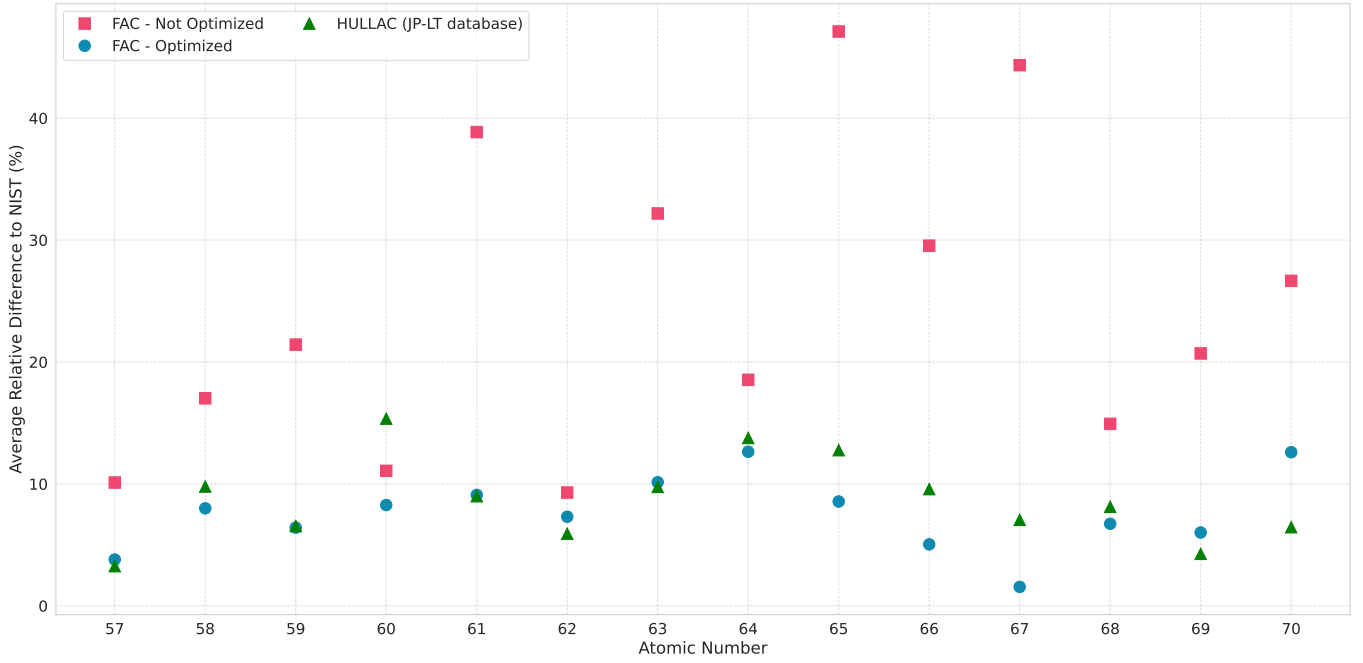


FIG. 14. Average relative difference to the experimental data available in the NIST ASD [27] for all singly ionized lanthanide ions computed with optimised FAC (in blue), compared with default FAC (in red) and calculations from the Japan-Lithuania opacity database for kilonova (2021) obtained with HULLAC (in green) [55]

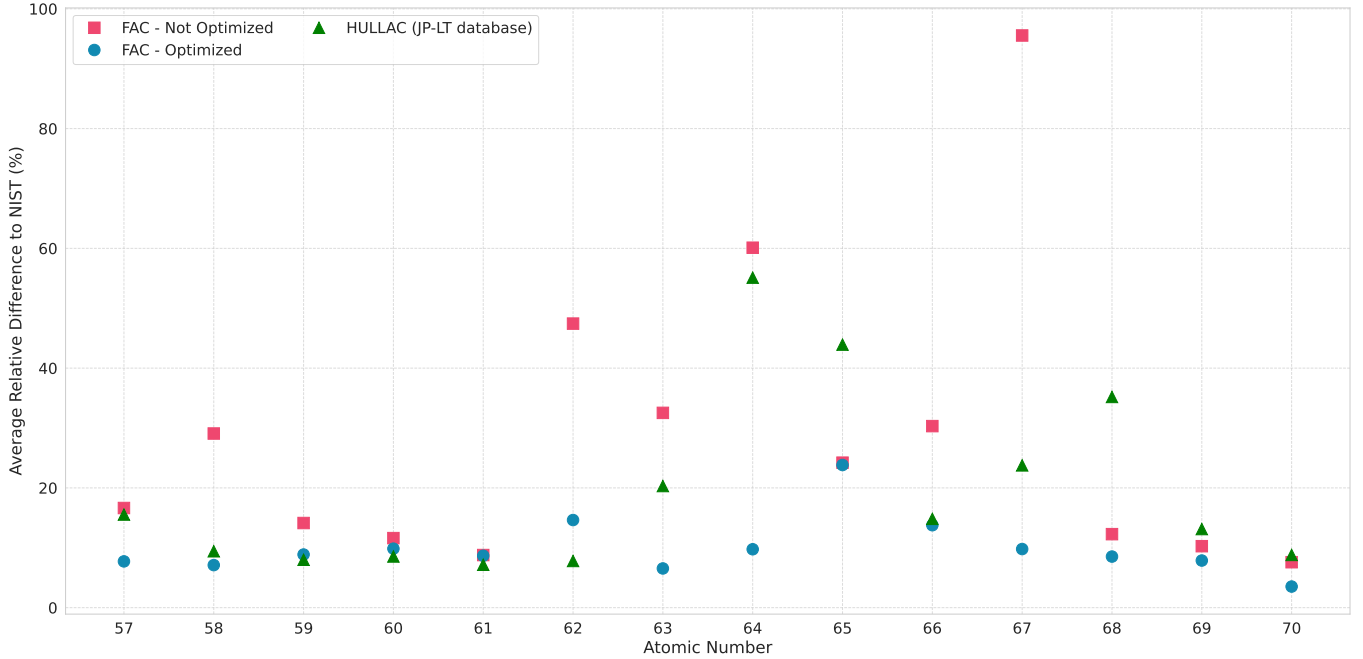


FIG. 15. Average relative difference to the experimental data available in the NIST ASD [27] for all doubly ionized lanthanide ions computed with optimised FAC (in blue), compared with default FAC (in red) and calculations from the Japan-Lithuania opacity database for kilonova (2021) obtained with HULLAC (in green) [55]